A Geodynamic Deformation Model of the Chuandian Region of Southeastern Tibet, with Constraints from GPS Data, Faults and Low-velocity Zones

Yudong Sun[1], Wei Leng[1, 2], Jing Liu-Zeng[3]

[1]Laboratory of Seismology and Physics of Earth's Interior; School of Earth and Space Sciences, University of Science and Technology of China, Hefei 230026, China.

[2]CAS Center for Excellence in Comparative Planetology, Hefei 230026, China.

[3]Institute of Surface-Earth System Science, Tianjin University, Tianjin 300027, China.

Corresponding authors: Yudong Sun (syd1997@mail.ustc.edu.cn)

Key points:

- We investigate the effects of the faulted shear zones and low-velocity zones on the horizontal GPS velocity field in SE Tibet
- The block extrusion model and crustal flow model may be both required to explain the tectonic activities
- Low-velocity zones are mechanically weak and possibly partially molten

Abstract

Southeastern Tibet is a key region for studying the tectonic evolution of Tibetan Plateau. The region is characterized by distributed faults, localized low-velocity zones (LVZs) in the mid-lower crust, and prominent clockwise rotation of GPS velocity field. End-member models have been proposed to explain the origin of this deformation pattern, including the block extrusion model highlighting the role of faulted shear zones, and the crustal flow model emphasizing the effect of a weak lower crust. Here we use a 3D visco-elasto-plastic finite element model to reproduce the instantaneous horizontal surface velocity and investigate the effects of active faults and LVZs on that. The results show that when only faults are included, the residual surface velocities between modeled and observed values are large at some locations overlying the LVZs; when only LVZs are included, the residual surface velocities along the Xianshuihe-Xiaojiang and Lijiang-Xiaojinhe faults, two major faults with relatively high slip rates, are significant. However, when both faults and LVZs are considered, the modeled surface velocities fit well with observed GPS velocities. Our results therefore demonstrate that a combination of fault-bounding block extrusion and crustal flow type of continuous deformation is required to explain the surface deformation. The model yields a high-resolution strain rate map which provides an improved understanding of Quaternary tectonics and seismic hazards. In order to reduce the residual velocities, the viscosity of LVZs is constrained as ~10^{20}-10^{21} Pa·s. Our study also suggests that LVZs are probably partially molten, which explains the rheology, seismological, and magnetotelluric data.

1. Introduction

Southeast Tibet, a mosaic of the Songpan-Ganzi Terrane, Sichuan Basin, Chuandian block, Shan-Thai Plateau, and the northern part of the Indochina block, is located on the southeastern borderland of the Tibetan Plateau, situated between the Burma subduction zone, Yangtze block and Sunda plate (Yin & Harrison, 2000; Pan et al., 2004). SE Tibet is often regarded as one of the most tectonically-active regions in the Asian continent (Figure 1a; Tapponnier et al., 1982, 2001; Wang, 1998; Deng et al., 2003; Zhang et al., 2003). A large topographic relief has been formed with a complex network of faults (Figure 1b; Clark & Royden, 2000; Liu-Zeng et al., 2008; Tapponnier et al., 2001; Taylor & Yin, 2009). Large earthquakes (Mw 7 or 8) have occurred in the region (Zhang & Liu, 1978; Chen & Wu, 1989; Xu et al., 2009; Xu et al., 2013; Yin et al., 2019). In addition, Tertiary-Quaternary magmatic activities have occurred in Tengchong (Wang et al., 2007), along the Red River fault (Wang et al., 2001) and in other areas, accompanied by high heat flux in much of Yunnan Province (Hu et al., 2000; Wang, 2001). As a result, the region has attracted much attention from researchers in terms of the study of seismic hazards, and because of the complexity of the geological systems.

A remarkable pattern of clockwise rotation of the horizontal velocity field around the eastern Himalayan syntaxis (EHS) has been observed in SE Tibet from modern geodetic measurements during the last few decades (Shen et al., 2005; Gan et al., 2007; Wang et al., 2016; Zheng et al., 2017). The GPS velocities decrease roughly with increasing radial distance from the EHS, and there are several large deformation centers along several major active faults and inside the blocks. The dynamic

mechanism of this surface deformation is still debated. And its relationships with geological structures, lithospheric rheology, and earthquake hazards are poorly understood.

Two main models have been proposed to explain the origin of this deformation pattern in SE Tibet: the block extrusion model (Tapponnier et al., 1982, 2001; Peltzer & Tapponnier, 1988; Avouac & Tapponnier, 1993) and the lower crustal flow model (Royden et al., 1997; Clark & Royden, 2000). In the extrusion model, the Shan-Thai, Indochina, Chuandian and Songpan blocks are extruded outwards, step by step, following the indention of the Indian Plate into the Eurasian Plate (Tapponnier et al., 1982; Peltzer & Tapponnier, 1988). The clockwise eastward extrusion results from the south-north shortening of central Tibet and the advance of the strong EHS (Panda et al., 2018). Specifically, the "bookshelf" model (England & Molnar, 1990) suggested that the deformation is conducted from the eastward extrusion to SE Tibet, via block rotation and fault slipping. The Shan-Thai block perhaps exemplifies a classic case of the "bookshelf" model (Wang, 1998; Tapponnier et al., 2001; Shi et al., 2018), with a nearly parallel series of left-lateral faults and two right-lateral faults (the Red River and Sagaing faults) on both sides (Figure 1b). Explicitly, the book-like blocks rotate clockwise when the Red River and Sagaing faults slip dextrally.

In order to explain both the simultaneous extension and uplift of Tibet and the surrounding highlands, such as the Songpan-Ganzi Terrane in SE Tibet (Liang et al., 2013), several researchers have emphasized the flow of the low viscosity lower crust as a channel, driven by Himalayan collision and the high-elevation topography of

Tibetan Plateau (Shen et al., 2005; Royden et al., 2008). In order to explain the northeastern and southeastern shunting of extrusion, the lower crustal flow is thought to be blocked by the strong Sichuan Basin (Clark and Royden, 2000; Cook & Royden, 2007). A lower crustal Poiseuille flow which is faster than the surface velocity can explain the gentle slope of the topography across the Chuandian block but a steeper slope across the margin of the Sichuan Basin (Clark & Royden, 2000; Clark et al., 2005; Burchfiel et al, 2008). Furthermore, from recent high-resolution seismic imaging (Yao et al., 2010; Bao et al., 2015), two low S-wave velocity zones (LVZs) are observed at depths from 10 km to 40 km, which are interpreted as two localized mid-lower crustal channel flows.

In addition to the block extrusion model and the lower crustal flow model, an asthenospheric flow model has also been proposed to explain the clockwise rotation (Becker & Faccenna, 2011; Magni et al. 2014; Huang et al., 2015; Sternai et al., 2016). However, the perturbation of surface deformation of a smaller scale triggered by asthenospheric flow may be much less than that triggered by faulted shear zones or crustal flow, due to the greater depth of the asthenosphere and the possible decoupling of lithosphere and asthenosphere (~100-200 km; Bendick & Flesch, 2013; Flesch et al., 2018).

High-accuracy long-term horizontal GPS data can be used as the constraint to evaluate the effects on the surface deformation pattern of either the fault network or the crustal flow. Several previous geodynamic models have been proposed to explain the velocity field in SE Tibet or across the whole of Tibet. The evolutionary models of

Tibet driven by the India-Eurasia convergence reproduce the clockwise rotation of the horizontal velocity field in SE Tibet (Cook & Royden, 2008; Yang & Liu, 2009; Chen & Gerya, 2016; Chen et al., 2017a). In order to obtain improved modeled velocity profiles for comparison with observed GPS data, geodynamic models for SE Tibet (Li et al., 2014; Zhu et al., 2016; Li et al., 2017b; Luo & Liu, 2018; Li et al., 2019b), or a larger region (Chen et al., 2016; Tunini et al., 2017; Bischoff & Flesch, 2018, 2019; Flesch et al., 2018) have been designed with imposed velocity boundary conditions. These models include one or more key factors, such as faults, weak lower crust, topographic gravitational energy, and block strength heterogeneities. In particular, Li et al. (2017b) regarded the lower crust as a viscous sheet for the entire region with an imposed fast velocity; however, this is contradicted by the localized LVZs revealed by seismic tomography (Bao et al., 2015). In addition, the model of Bischoff & Flesch (2018) includes the lower crustal flow in central Tibet constrained by seismic tomography, and it provides a better fit to the GPS velocity data, except for SE Tibet. Li et al. (2019b) suggested that gravitational spreading is the major cause of the horizontal velocity field, but the viscosity of the upper crust used in their model is relatively low (~0.8-4×10^{21} Pa·s). Therefore, a high resolution model of SE Tibet with a more accurate structure of faults and LVZs is needed to determine a more precise mechanism for the observed deformation pattern.

2. Model setup

2.1. Geodynamic model

We used a 3D visco-elasto-plastic finite element model (Figure 2a; Moresi et al.,

1996, 2003; Leng & Gurnis, 2011, 2015), including crustal and lithospheric heterogeneities, faults, and LVZs, to reproduce the instantaneous horizontal surface velocity and examine the effects of faulted shear zones and LVZs on that. The model solves the three conservative equations of mass, momentum and energy, with Boussinesq approximation and the infinite Prandtl number:

$$v_{i,i} = 0 (1)$$

$$-p_{,j}\delta_{ij} + \tau_{ij,j} = \Delta\rho g\delta_{i3} (2)$$

$$\rho C_p\left(\dot{T} + v_i T_{,i}\right) = \left(kT_{,i}\right)_{,i} (3)$$

Here, $v_i, p, \tau_{ij}, \Delta\rho, g, \rho, C_p, T, k,$ and δ_{ij} are respectively the velocity vector, pressure, deviatoric stress tensor, density anomaly, gravitational acceleration, density, specific heat capacity at constant pressure, temperature, thermal conductivity, and the Kronecker function. For simulation of viscoelastic deformation, we considered the crust and mantle as a Maxwell fluid, as follows:

$$\dot{\varepsilon}_{ij} = \frac{1}{2G}\dot{\tau}_{ij} + \frac{1}{2\eta}\tau_{ij} (4)$$

where $\dot{\varepsilon}$, $\dot{\tau}$, τ, G, and η are respectively the tensors of strain rate, stress rate, stress, shear modulus, dynamic viscosity, and i, j represent spatial indices.

We used a power law relation to describe the temperature-dependent viscosity of the lithosphere (Karato & Wu, 1993), as follows:

$$\eta = \eta_0 \left(\frac{\dot{\varepsilon}_{II}}{\dot{\varepsilon}_0}\right)^{\left(\frac{1}{n}-1\right)} exp\left(\frac{E}{nR}\left(\frac{1}{T} - \frac{1}{T_0}\right)\right) (5)$$

where η_0, $\dot{\varepsilon}_{II}$, $\dot{\varepsilon}_0$, n, E, R, T, and T_0 are respectively the reference viscosity, second invariant of the deviatoric strain rate tensor, reference strain rate, strain exponent, activation energy, gas constant, and absolute and reference temperatures (Table 1). For diffusion creep within the asthenosphere (Karato, 2010), we used a constant

viscosity of 10^{19} Pa·s. In addition, the transition from viscous creep to failure can be reproduced by strain weakening effects. The strain weakening and strain-rate weakening effect (non-Newtonian creep) both lubricate the shear zones (Tackley, 2000), and may promote the change of deformation from a brittle to ductile style within the fault zone (Niemeijer et al., 2010). In our model, the effect of plastic strain weakening was incorporated by decreasing the yielding stress with the accumulation of plastic strain (Poliakov & Buck, 1998; Leng & Gurnis, 2011, 2015), as follows:

$$\tau_f = \mu P + C \quad (6)$$

$$\mu = \mu_0 - \mu_0 min\left(1, \frac{\varepsilon_p}{\varepsilon_f}\right) \quad (7)$$

$$C = C_0 - (C_0 - C_f) min\left(1, \frac{\varepsilon_p}{\varepsilon_f}\right) \quad (8)$$

Here, $\tau_f, P, \mu, \mu_0, \varepsilon_p, \varepsilon_f, C_0, C_f$, and C are respectively the yield stress, pressure, coefficient of friction, initial coefficient of friction, accumulated plastic strain, reference plastic strain, initial cohesion, minimum cohesion, and cohesion (Table 1).

Different rheology profiles were set for the faulted shear zones and continental lithosphere with or without a weaker mid-lower crust (Figure 2b). The strength profile of the lithosphere without LVZs follows the crème-brûlée model (Kohlstedt et al., 1995), and the initial frictional coefficient, initial and minimum cohesion of friction (μ_0, C_0, and C_f) were set to 0.5, 40 MPa and 0.6 MPa, respectively (Table 1). For the strength profile of the faulted shear zones, only the yield stress was changed (μ_0, C_0 and C_f were set to 0.001, 4 MPa and 0.6 MPa, respectively), suggesting a pre-existing fracture zone, or the occurrence of fluid, partial melting or weak minerals within the fault zone (Collettini et al., 2009; Niemeijer et al., 2010; Carpenter et al., 2011; Lockner et al., 2011; Gao & Wang, 2014). Notably, the variation of viscosity with

170 depth for faulted shear zones is still temperature- and stress-dependent and therefore it
171 varies between faults. The strength profile for the lithosphere with LVZs follows the
172 jelly sandwich model (Kohlstedt et al., 1995), with a lower constant viscosity for the
173 LVZ (Figure 2b).

174 The 3D Cartesian model (Figure 2a; Table 1) covers the area of the rectangle
175 shown in Figure 3a by transverse Mercator mapping. We used 120×82×28 elements
176 with 108 particles initially deployed in each element for tracking the material
177 properties and strain history (Leng & Gurnis, 2011, 2015). Vertically, it is divided
178 into four layers: a sticky air layer of 20 km, crust layer, mantle lithosphere, and
179 asthenosphere layer down to the depth of 282 km. The density of the crust and mantle
180 was set to 2.7 g/cm^3 and 3.3 g/cm^3, respectively. The initial thermal structure is
181 controlled mainly by lithosphere thickness, as a linearized distribution of temperature
182 varying with depth within the lithosphere, and a constant temperature for the
183 asthenosphere.

184 The high topography of Songpan-Ganzi terrane can be reproduced by including
185 different depths of Moho and LAB (see section 2.2.1 for the details) and the sticky air
186 layer after the model reaches isostacy. Therefore, the lithospheric deformation can be
187 driven by the gravitational potential energy.

188 Since the tectonic force of continental plates is derived from within the
189 lithosphere rather than from the asthenosphere, we applied driving forces in the model
190 via imposed lateral boundary velocities in the lithosphere (see section 2.2.2 for an
191 explanation of how we obtained the imposed lateral boundary velocities from GPS

192 data). The boundary condition of horizontal velocities was applied to lithospheric
193 sections on the four lateral walls of the box, which are constant with depth due to the
194 large viscosity of the lithosphere. Free-slip boundary conditions were used at
195 asthenospheric sections.

196 **2.2. Input data from observations**

197 **2.2.1. Crustal and lithospheric thickness**

198 The Moho depth map used in our model is from Yang et al. (2020) (Figure 2c).
199 And the lithospheric thickness is from Litho 1.0 (Figure 2d; Pasyanos et al., 2014),
200 which were obtained by iterating to fit the surface wave dispersion curves; it is well
201 correlated with the distribution of elastic thickness (Audet & Bürgmann, 2011).

202 **2.2.2. GPS data**

203 396 interseismic GPS data from SE Tibet (black arrows in the rectangle in Figure
204 3a; Zheng et al., 2017) for 1991 to 2015 were used as the observed surface velocities
205 and were compared with the modeled surface velocities. Furthermore, the laterally
206 imposed velocity boundary condition in the lithosphere is a key factor influencing the
207 surface deformation pattern. Previous geodynamic models typically interpolated the
208 GPS data to predefined meshes on the lateral boundaries; however, the GPS stations
209 are sparsely distributed on the box boundaries (Figure 3a) which reduces the accuracy
210 of the interpolation. Therefore, we computed the lateral boundary velocities based on
211 the “Blocks” model (Meade & Loveless, 2009), by this method which considers more
212 geological structural information. In this way, we first constructed a closed block and
213 fault network (the thin black lines in Figure 3a) based on the fault system collected by

Taylor & Yin (2009) (purple lines in Figure 3b). We then used 2576 GPS data from Zheng et al. (2017) to invert for the rotating rate of each block and backslip rate of each fault. From these two sets of parameters, the lateral boundary velocities on the margin of the study area were calculated and are shown in Figure 3b.

2.2.3. Faults

Our fault model for SE Tibet was constructed based on fault traces, earthquake locations, and focal mechanisms (Figure 4a, 4b and 4c). Active faults in the Holocene were compiled as a combination of several studies (Zhang et al., 2003; Taylor & Yin, 2009; Wu et al., 2018; Shi et al., 2018), and earthquake locations were used to supplement the recognition of fault traces. Several faults with changes in strike were simplified with segmented straight lines.

The dip angle of faults was inferred from seismic reflection profiles (Li et al., 2010) and the focal mechanisms of recorded earthquakes occurring on the faults. Records of focal mechanisms were collected from the Global CMT (https://www.globalcmt.org; Ekström et al., 2012) and the China Earthquake Data Center (http://data.earthquake.cn; Figure 4a), for 1966 to 2017. For each segment of a fault, the dip angle was represented by the average rupture plane of adjacent earthquake (distance < 20 km) and nearly parallel to the fault strike direction (intersecting angle < 30°).

The fault locking depth was calculated following the method for determining the seismogenic zone (Smith-Konter et al., 2011), which includes 95% of the total earthquakes nearby (< 5 km), defining the boundary of seismic and aseismic zones.

Earthquake logs (Figure 4b) were downloaded from IRIS (http://ds.iris.edu/wilber3/, from 1968 to 2018, with magnitude > 4) and the China Earthquake Data Center (http://data.earthquake.cn, from 1968 to 2019, with magnitude > 2).

We used a finite-thickness weak zone to simulate the faulted shear zone, following the examples of Hearn et al. (2002; 2009) and Johnson & Segall (2004). Our fault model consists of a thin faulted shear zone of 11 km thickness above the locking depth, and a thicker shear zone from the locking depth to the Moho, representing the plastic creeping zone (Figure 4d). With regard to the upper part of the faulted shear zone (i.e. above the locking depth), we set the dip angle as discussed above; for the lower part (i.e. beneath the locking depth), we assumed that the dip angle equals 90° (Figure 4d).

2.2.4. Tomography of the LVZs

Numerous studies of the seismic tomography of the crust and mantle structure in SE Tibet have been conducted over the last decade, using different inversion methods such as P waves (Wei et al., 2013; Yang et al., 2014; Huang et al., 2018), surface waves (Chen et al., 2014; Wang et al., 2014; Bao et al., 2015; Wu et al., 2016; Shen et al., 2016), and full waveforms (Chen et al., 2017b; Tao et al., 2018). With the improved resolution of seismic imaging, two LVZs of both P and S waves in the crust are illustrated in all models, although there are differences in detail between different models. In general, one LVZ spreads from the Songpang-Ganzi Terrane, across the Lijiang and Dali basins, to Western Yunnan; and the other extends along the Xiaojiang fault and across the Red River fault to the Simao Terrane (Figure 5). These

two LVZs are spatially divided by the inner core of the Emeishan large igneous province in Panzhihua-Xichang region (Chen et al., 2015).

Considering scale and resolution, we chose two models of S-wave tomography for application in the study: Tao_2018 by full waveform inversion (Tao et al., 2018, Figure 5a), and Shen_2016 by ambient noise inversion (Shen et al., 2016, Figure 5b). The shapes of LVZs were contoured according to S-wave velocity anomalies. For each depth, if the S-wave velocity anomaly was lower than a threshold, as $dVs/Vs < -r * \sigma$, where r and σ are the ratio and standard deviation of velocity anomaly, it was defined as an LVZ (Figure 5c and 5d). In addition, the low S-wave velocity layer from 0 to 10 km provides information about the sediment layer within the Sichuan Basin and therefore it was excluded from the model. Geophysical observations show that these LVZs are characterized by low electrical resistivity (Bai et al., 2010), high attenuation (Zhao et al., 2013), high Poisson's ratio (Chen et al., 2013; Sun et al., 2014; Tao et al., 2018), and high heat flow (Hu et al., 2000). Low S-wave velocity and a higher Poisson's ratio may indicate the presence of partial melting and the reduction of viscosity (Takei, 2002; Brantut & David, 2018), and therefore in the model we used the prescription that LVZs had a uniform lower viscosity, which was later optimized in the modeling.

3. Results

3.1. Impacts of faults and LVZs on surface deformation

Both faulted shear zones and LVZs are regarded as "defects" in continents. The strain resulting from screw dislocation of the planar "defect" is proportional to $1/r^3$,

where r is the distance from the "defect" to the observation location (Savage & Burford, 1973; Okada, 1985; Landau & Lifshitz, 1986); therefore, we infer that the impacts of faults and LVZs are limited to the area surrounding them. After applying the velocity boundary conditions and gravitational potential energy, these "defects" can be detected in GPS measurements by examining the residual velocity, which is equal to the modeled velocity minus the observed velocity. We attempted to minimize the residual velocity by testing scenarios of various geological settings in the modeling, and the parameterizations with the best degree of fit were considered to be estimates of the properties of the underground structure.

The residual velocity fields were computed when the model reached topographic isostacy after stress relaxation. The distributions of the values of the root mean square (RMS) of the residual velocity in five models are illustrated in Figure 6 and their settings are specified in Table 2. In Figure 6a, the reference case (case_ref) without faults and LVZs was unable to produce sufficient clockwise rotation at the Chuandian, Western Yunnan and Simao Blocks, and there were relatively large residual velocities across the entire area. When only faults were included into the model (case_fault, Figure 6b), the residual velocities decreased significantly, but there were still some areas with relatively large residual velocities. It is interesting to note that the distribution of large residual velocities is similar to the distribution of two LVZs (Ganzi, Lijiang, and Tengchong; Kunming, Chuxiong, and Simao). On the other hand, when only LVZs with a viscosity of 10^{20} Pa·s were included into the model (case_LVZs, Figure 6c), the remaining part with large velocity misfits occurred along

the Xianshuihe-Xiaojiang fault and Lijiang-Xiaojinhe fault, which are two active shear zones with large slip rates. When both faults and LVZs were included in the model, two cases (case_both1 and case_both2) where the LVZs are respectively constrained by two different tomography models (Tao_2018 and Shen_2016 in Table 2) provide better fits of the surface motion in most locations (Figure 6d and 6e). The results clearly demonstrate that faulted shear zones and localized LVZs are the two most important factors, which jointly influence the velocity field in SE Tibet. Notably, the model with only one factor exhibits poor GPS fitting at the location of the other (Figure 6b and 6c).

3.2. Estimating the structure and rheology of faults and LVZs

We tried to provide a rough estimate of the thickness of the lower faulted zones, using the model of faulted shear zones described above (section 2.2.3; Figure 4d). Seismic and magnetotelluric data across the faults show that there are related weak zones below the surface, but the thickness of these lower faulted zones are not well constrained due to the low resolution and smearing effects of tomographic maps (Li et al, 2019a; Yang & Duan, 2019). In case_fault (Table 2), when the thickness of the lower faulted zone was increased from 11 km to 45 km, the RMS of the residual velocity decreased rapidly at first, and then more slowly when the thickness of the lower faulted zone reached ~22 km (Figure 7a). Therefore we estimate that the thickness of the lower part of the faulted shear zone may be around 22 km for our model, which reproduced the observed surface ground motion. Admittedly, There is trade-off between the rheology and the thickness of faulted shear zones, and the yield

stress is not well constrained. Thus, this estimation may not indicate the actual thickness of faulted shear zones.

In a similar way, we estimated the size and viscosity of LVZs, since they are important to understand how the mid-lower crust deforms in response to tectonic forces. Specifically, whether the LVZs (Figure 5a and 5b) are connected to each other is greatly debated, due to the small-scale differences between the seismic tomography results for SE Tibet (Wei et al., 2013; Bao et al., 2015; Shen et al., 2016; Huang et al., 2018).

In case_both1 and case_both2, we first fixed the viscosity of the LVZs to 10^{20} Pa·s and adjusted their size by changing the ratio r (defined in section 2.2.4). In Figure 7b, the RMS of the residual velocity reaches a minimum value with the volume of ~1.4-1.6×10^7 km^3. The resulting best fit models for Tao_2018 and Shen_2016 are illustrated in Figure 5c and 5d, respectively. The RMS became very large, as the size increased, two LVZs merged into one and the connections were wide enough to conduct flow. Therefore, two LVZs are generally isolated, and it is unlikely for the northwestern LVZ to flow southeastward to the other LVZ. Both best-fitting results show a narrow connection between LVZs below the Chuxiong fault in the southwest, but there is no connection at the shallow part (~10-km depth) at Xichang in the northeast. Whether or not there is a connection in the lower part below Xichang remains unclear, due to the difference in these two tomography models. With the size of LVZs obtained in Figure 7b, the results of the RMS of the residual velocity versus viscosity are illustrated in Figure 7c. It can be observed that in order to obtain the

346 minimum residual velocity, the viscosity for the LVZs needs to be within the range of
347 ~10^{20}-10^{21} Pa·s.

348 **3.3. Map of the strain rate**

349 In order to analyze the local tectonic processes in SE Tibet, we chose the ideal
350 model (case_both1, Figure 6d) and computed the first-order derivative of the velocity
351 field in order to obtain maps of the strain rate tensor, maximum shear strain rate,
352 extension strain rate, and vorticity (rotational strain rate) (Figure 8a, 8c, 9a and 9c,
353 respectively). They are compared with the corresponding strain maps (Figure 8b, 8d,
354 9b and 9d) which are smoothed by meshes of 0.2^{o} (latitudinal) by 0.25^{o} (longitudinal)
355 from the observed GPS data (Kreemer et al., 2014; lacking for the Sichuan Basin).
356 Essentially, our modeled strain rate maps successfully reproduced the observed
357 deformation pattern. The magnitude and direction of the strain rates approximate the
358 observed rates (Figure 8a and 8b), and the sense of strike-slip fault is consistent with
359 geological observations (Figure 9c and 9d).

360 Based on the magnitude of the clockwise rotation, SE Tibet can be divided into
361 three sub-regions (Figure 9c and 9d): (i)Northern Myanmar, the Sanjiang region, and
362 Western Yunnan; (ii) the Songpan-Ganzi Terrane, Chuandian Block, and the Simao
363 Terrane; (iii) the Sichuan Basin, South China, and the Sunda plate. The vorticity
364 decreases from the interior to the outside, bounded by the Litang-Chenghai-Longling-
365 Ruili fault and the Xianshuihe-Xiaojiang fault. The clockwise rotation of regions (i)
366 and (ii) is probably due to the east- to southeast-ward extrusion from Tibet, and the
367 anti-clockwise rotation of region (iii) may be due to extension resulting from the

Sunda or Pacific subduction (Shen et al., 2005).

In the extension strain rate map (Figure 9a and 9b), the model reveals extension in the Chuandian block and compression in the Longmenshan region. It also demonstrates staggered grids of extension and compression along several active faults, such as the Xianshuihe-Xiaojiang fault, which possibly result from variable slip rate along the fault. Several localized extensional zones may explain the formation of basins such as the Tengchong, Dayingjiang and Ruili basins in Western Yunnan, Lijiang, Jianchuan, Eryuan, Binchuan, and the Chenghai basins around the diamond-shaped Lijiang-Dali block, Zhongdian and Litang basins (green outlines; Fgiure 9a and 9b).

Distinct shear strain rates are evident along two chains of active faults in the model (Figure 8c) and they match the observations (Figure 8d). One is the arcuate Xianshuihe-Xiaojiang and Dien Bien Phu faults, and the other is the Lijiang-Xiaojinhe, Longling-Ruili and Dayingjiang faults. In addition, in the Simao Basin, a "tail" of shear deformation is evident extending westward from the curved Xianshuihe-Xiaojiang fault (Figure 9c). Since no NE-trending faults coincide with the high shear strain zone, it is possibly caused by the underlying LVZ.

Admittedly, the modeled maps do not exactly match the observed maps, especially in terms of the magnitude of the maximum shear strain rate (Figure 8c). This may be attributed to the smearing problem during the interpolation of the still sparse GPS data (Figure 8d). For example, the modeled shear strain rates of the Longriba, Litang and Nantinghe faults are much higher than the observed rates from

GPS. However, the higher shear strain rates shown by the model appear to be compatible with geologic observations. For instance, the geological average slip rate of the Longriba fault is 7.5 mm/yr during the latest Pleistocene and 2.1 mm/yr in the Holocene (Ren et al., 2013); the slip rate on the Litang fault is 2.3 mm/yr during the last 173 kyr (Chevalier et al., 2016) and 4 mm/yr in the last 14 kyr (Xu et al., 2005); the Nantinghe fault slips is 4 mm/yr (Shi, 2014).

4. Discussion

Compared with previous models which simulate continental deformation, our high-resolution model considers combined effects of different thicknesses of crust and lithosphere, temperature-dependent non-Newtonian rheology, a realistic 3D fault network, and tomography-based LVZs. Specifically, the heterogeneity of the strength of different blocks can be reproduced by different thicknesses and temperature-dependent rheology. The boundary condition is applied to the entire lithosphere using horizontal velocities inverted from interseismic GPS data, and the isostatic topography can be produced with a sticky air layer in our model. Therefore, our lithosphere model is driven by both tectonic forces and topographic gravitational potential energy. Admittedly, the boundary and initial conditions are still over simplified; plus, the rheology, temperature, and density of the lithosphere are largely unclear; and the structure and depth of faulted shear zones at greater depths are not well constrained. Thus it was difficult to use the model to study the deformation of deeper structure in detail. Notably, a perfect fit of GPS data is impossible and therefore our intention is to study the major features in tectonics with the focus on the

412 factors controlling deformation.

413 **4.1. Block extrusion model vs. lower crust flow model**

414 The two prevailing models of the geodynamics of SE Tibet, the rigid block
415 extrusion model and the lower crustal flow model, both are able to explain parts of the
416 history of regional tectonic evolution, together with geophysical observations. The
417 rigid block extrusion model emphasizes localized strike-slip deformation along active
418 faults and oblique convergence at the plateau margin, while the lower crustal flow
419 model suggests more continuous deformation driven by viscous lower crustal flow.
420 From our perspective, since the deformation in the upper crust is unarguably
421 dominated by faults, the key point of the debate is, whether deformation of the lower
422 crust is dominated by localized shear zones or by regionally distributed lower crustal
423 flow. Since the LVZs and faulted shear zones can be observed by seismological and
424 magnetotelluric tomography, accompanied by the GPS modeling in this study (section
425 3.1; Figure 6), we argue that the rigid block extrusion model and lower crustal flow
426 model may be both required for SE Tibet.

427 **4.1.1. Geodynamic implications: faults and LVZs**

428 First, our interpretation is supported by several observations from the strain rate
429 maps and tectonics. One proof is the NE-trending “tail” (Figure 9c) in the Simao
430 Terrane, which might be the result of left-lateral shear deformation of the LVZ at
431 depth extending from the Xiaojiang fault across the Red River fault. This indicates
432 that deformation occurs in the mid-lower crust where no NE-trending faults have
433 developed, and a similar example is the “tail” extending from the Lijiang-Xiaojinhe

434 fault at Baoshan. Second, our arguments are supported by the low slip rate and
435 inactive seismicity at the Red River fault, but the higher slip rate and greater
436 seismicity at the parallel Chuxiong fault (Figure 4b and 8d). This is probably because
437 the connection between the two LVZs is localized beneath the Chuxiong fault (Figure
438 5a and 5b), and because the right-lateral shear rate shifts from the Red River fault to
439 the adjacent Chuxiong fault.

440 At a larger scale, two localized channel flows cause rapid southwestward motion:
441 one is from Songpan-Ganzi Terrane, along the Lijiang-Xiaojinhe fault to Baoshan city;
442 and the other is from the Xiaojiang fault to the Simao Terrane (Figure 6b and 9c). The
443 existence of these two channel flows is also verified by the southwestern bulge of the
444 Lancang River at Baoshan (Socquet & Pubellier, 2005) and the Red River,
445 Babianjiang and Wuliangshan faults in the Simao Terrane (Schoenbohm et al., 2006).
446 Due to these two LVZs branch from the arcuate Xianshuihe-Xiaojiang-Dien Bien Phu
447 fault, the slip rate of these three faults decreases from north to south (~15, 10, 3
448 mm/yr). In addition, the direction of flow motion is largely determined by the
449 structure of the LVZs, since they are isolated by the bounding strong terranes. Due to
450 the very limited connection between the two LVZs and the terminus of the LVZ at the
451 boundary of the South China and Chuandian Blocks, the crustal flow migrates to the
452 southwest but not to the southeast.

453 **4.1.2. The bookshelf model**

454 The well-known bookshelf model in the Shan-Thai Plateau was previously
455 described as a series of rotating parallel rectangular blocks confined by two right-

456 lateral strike slip faults (the Red River and Sagaing faults) (Leloup et al., 1995;
457 Lacassin et al., 1997, 1998; Tapponnier et al., 2001). However, this model cannot
458 explain the absence of obvious northward motion of the blocks driven by the large
459 slip rate of the Sagaing fault (~18 mm/yr; Maurin et al., 2010) and rather slow slip
460 rate of the Red River fault (~1-2 mm/yr; Shen et al., 2005) (Figure 3a). Therefore, the
461 left-lateral strike-slip faults in the bookshelf model may be driven by the paralleling
462 shear from the northwestern LVZ on the northern margin (Tengchong).

463 The actual tectonic map may be more complex than the model. At the
464 northeastern side of the Lancang-Mengzhe fault in the Simao Terrane, there are
465 several NW-trending right-lateral faults, but few NE-trending, left-lateral faults
466 (Figure 1b). This can be explained by localized deformation in the underlying LVZ
467 (discussed in the section 4.1.1), which may transfer the localized left-lateral
468 deformation along the Xiaojiang fault southwestward to the more distributed faults
469 (Figure 9c and 9d).

470 **4.2. Revision on crustal flow: rheology and partial melting**

471 The lower crustal layer in the crustal flow model is typically regarded as a
472 widespread weak sheet in the jelly sandwich model. However, Jackson (2002) argued
473 that the presence of the weak crustal layer can only be ascribed to additional partial
474 melt or fluid. In addition, small-scale low anomalies in the seismic tomography of
475 Tibetan crust are often thought to be the result of this type of chemical anomaly
476 (Hacker et al., 2014). Therefore, an alternative means can be used to define the lower
477 crustal flow: as the localized LVZs constrained by seismic tomography. In this

approach, the crustal flow is at a much shallower depth of the middle crust (~10-40 km) and does not reach the Moho discontinuity. The absence of LVZs beneath the Sichuan Basin and Panzhihua-Xichang (Figure 5) may account for the large topographic relief at their northwestern periphery (Figure 1a; Clark et al., 2005). Therefore the localized LVZs blocked by the surrounding strong terranes may not flow as was once believed (Clark & Royden, 2000). They may be only able to migrate with the assistance of the relative motions of the blocks and the deformation in the faulted shear zones.

The viscosity of the mid-lower crustal flow is an important parameter that determines how the entire lithosphere deforms in response to gravitational loading and tectonic forces. Our estimation of viscosity (~10^{20}-10^{21} Pa·s; section 3.2; Figure 7c) suggested that LVZs may not be as weak as researchers once thought (Figure 10a; ~10^{18} Pa·s, Clark & Royden, 2000). However, there are significant differences between the results obtained by different geodynamic models (Figure 10a; Clark & Royden, 2000; Flesch et al., 2001; Jiménez-Munt & Platt, 2006; Zhang et al., 2009; Shao et al., 2011; Yin & Taylor, 2011; Zhu & Zhang, 2013; Huang et al., 2014; Xu et al., 2014; Shi et al., 2015; Xu et al., 2016; Diao et al., 2018; Bischoff & Flesch, 2018; Panda et al., 2019; Wang et al., 2019). It is worth noting that, the models may give larger values for viscosity with a smaller strain rate (larger timescale), from post-seismic (decades), lake-shoreline rebound (thousands of years), to geodynamics (millions of years). Therefore, it suggests that mid-lower crust could be regarded as non-Newtonian fluid, and the deformation of that may be dominated by dislocation

creep. This rate-dependent rheology may be the major reason for the differences of viscosity estimations.

In order to know the current status of LVZs, we evaluated whether partial melting is required to explain the estimated viscosity in this study. First, the temperature profiles for the crust of the Sichuan Basin, Panzhihua-Xichang, Dali (northwestern LVZ), and Kunming (southeastern LVZ) were calculated as a two-layer model constrained by two sets of data, heat flow and thermal conductivity from the International Heat Flow Commission (IHFC; http://www.ihfc-iugg.org/products/global-heat-flow-database; Wang & Huang, 1987; Hu et al., 2000; Wang, 2001), and were constrained by the depth of the Curie surface as well (Figure 10b; Hemant & Mitchell, 2009; Gao et al., 2015). As seen in Figure 10b, the temperature for dehydration melting is reached for the middle crust of LVZs.

Second, the viscosity profiles for wet quartzite, wet feldspar and partially molten wet granite were illustrated in Figure 10c according to the temperature profiles of two LVZs (Hirth et al., 2001; Rutter & Brodie, 2004; Rutter et al., 2006; Rybacki et al., 2006; Bürgmann & Dresen, 2008). Thus the viscosity of the mid-lower crust beneath wet solidus is too low to be explained by structural water and is likely to be partially molten.

In addition, partial melting is needed to explain the low electrical resistivity of the LVZs (~3-10 Ω·m; Bai et al., 2010; Rippe & Unsworth, 2010; Zhao et al., 2012; Dong et al., 2016; Cheng et al., 2019; Li et al., 2019a; Xue et al., 2019; Zhao et al., 2019), based on the measurements of hydrous peraluminous granitic melt (Guo et al.,

2018). The high Poisson's ratio of the LVZs (Li et al., 2017a; Deng et al., 2018; Tao et al., 2018) indicates partial melting as well (Takei, 2002; Brantut & David, 2018). In conclusion, the LVZs in the mid-lower crust are partially molten, which possibly results from both the high temperature and dehydration of hydrous minerals.

5. Conclusions

We presented a 3D geodynamic model of Chuandian region to reproduce the instantaneous horizontal surface velocity driven by tectonic forces and topographic gravitational energy. The detailed GPS velocity pattern may represent a joint contribution from both faulted shear zones and two localized LVZs. This result may indicate that the block extrusion model and lower crustal flow model are not mutually exclusive and both required for explaining the SE Tibetan tectonics. We provided additional constraints on the size and viscosity of tomography-based LVZs. These results suggest that weak LVZs are bounded by surrounding strong terranes, flow southwestward and possibly contribute to the clockwise movement of upper crust. The strain rate maps from the best-fit model could give some clues into complex deformation of strike-slip faults and extensional basins in SE Tibet. In addition, the estimation of the viscosity of LVZs (10^{20}-10^{21} Pa·s) suggests that rocks are probably partially molten, due to the high temperature and dehydration.

Acknowledgments

We appreciate constructive comments from two anonymous reviewers. We are grateful to Roland Bürgmann, Huajian Yao, Renqi Lu, Xuhua Shi, Ling Chen, Xuan Guo, Yan Hu, Hua Wang, Zhiqi Zhang and Shuye Huang for their advice and help.

This research is supported by the National Natural Science Foundation of China (awards 41774105, 41820104004, 41688103) and the Sichuan-Yunnan National Earthquake Monitoring and Forecasting Experimental Site Project (Grant No. 2017CESE0102). Generic Mapping Tools (GMT) was used to generate many figures in this paper. All of our data come from previously published sources. Seismic data used in the simulations is available through Litho 1.0 (Pasyanos et al., 2014), Shen et al. (2016), Tao et al. (2018) and Yang et al. (2020). Data used in the construction of fault model is available through the Global CMT (https://www.globalcmt.org; Ekström et al., 2012), the China Earthquake Data Center (http://data.earthquake.cn), IRIS (http://ds.iris.edu/wilber3/), the Earth Observation from Space Data Sub-center (http://data.cea-ies.ac.cn) and Taylor & Yin (2009). The GPS data is available from online supplements of Zheng et al. (2017) and Kreemer et al. (2014). The heat flow data is available through the International Heat Flow Commission (IHFC; http://www.ihfc-iugg.org/products/global-heat-flow-database).

References

Audet, P., & Bürgmann, R. (2011). Dominant role of tectonic inheritance in supercontinent cycles. *Nature Geoscience*, 4(3), 184. https://doi.org/10.1038/ngeo1080

Avouac, J. P., & Tapponnier, P. (1993). Kinematic model of active deformation in central Asia. *Geophysical Research Letters*, 20(10), 895-898. https://doi.org/10.1029/93GL00128

Bai, D., Unsworth, M. J., Meju, M. A., Ma, X., Teng, J., Kong, X., ... & Zhao, C. (2010). Crustal deformation of the eastern Tibetan plateau revealed by magnetotelluric imaging. *Nature geoscience*, *3*(5), 358-362. https://doi.org/10.1038/ngeo830

Bao, X., Sun, X., Xu, M., Eaton, D. W., Song, X., Wang, L., ... & Huang, Z. (2015). Two crustal low-velocity channels beneath SE Tibet revealed by joint inversion of Rayleigh wave dispersion and receiver functions. *Earth and Planetary Science Letters*, 415, 16-24. https://doi.org/10.1016/j.epsl.2015.01.020

Becker, T. W., & Faccenna, C. (2011). Mantle conveyor beneath the Tethyan collisional belt. *Earth and Planetary Science Letters*, 310(3–4), 453–461. https://doi.org/10.1016/j.epsl.2011.08.021

Bendick, R., & Flesch, L. (2013). A review of heterogeneous materials and their implications for relationships between kinematics and dynamics in continents. *Tectonics*, 32(4), 980-992. https://doi.org/10.1002/tect.20058

Bischoff, S. H., & Flesch, L. M. (2018). Normal faulting and viscous buckling in the Tibetan Plateau induced by a weak lower crust. *Nature communications*, 9(1), 4952. https://doi.org/10.1038/s41467-018-07312-9

Bischoff, S., & Flesch, L. (2019). Impact of Lithospheric Strength Distribution on India-Eurasia Deformation From 3-D Geodynamic Models. *Journal of Geophysical Research: Solid Earth*, 124(1), 1084-1105. https://doi.org/10.1029/2018JB015704

Brantut, N., & David, E. C. (2018). Influence of fluids on VP/VS ratio: increase or decrease?. *Geophysical Journal International*, 216(3), 2037-2043. https://doi.org/10.1093/gji/ggy518

Burchfiel, B. C., Royden, L. H., van der Hilst, R. D., Hager, B. H., Chen, Z., King, R. W., et al. (2008). A geological and geophysical context for the Wenchuan earthquake of 12 May 2008, Sichuan, People's Republic of China. *GSA Today*, 18(7), 4– 10. doi: 10.1130/GSATG18A.1

Bürgmann, R., & Dresen, G. (2008). Rheology of the lower crust and upper mantle: Evidence from rock mechanics, geodesy, and field observations. *Annu. Rev. Earth Planet. Sci.*, 36, 531-567. https://doi.org/10.1146/annurev.earth.36.031207.124326

Carpenter, B. M., Marone, C., & Saffer, D. M. (2011). Weakness of the San Andreas Fault revealed by samples from the active fault zone. *Nature Geoscience*, 4(4), 251. https://doi.org/10.1038/ngeo1089

Chen, L., Capitanio, F. A., Liu, L., & Gerya, T. V. (2017a). Crustal rheology controls on the Tibetan plateau formation during India-Asia convergence. *Nature communications*, 8, 15992. https://doi.org/10.1038/ncomms15992

Chen, L., & Gerya, T. V. (2016). The role of lateral lithospheric strength heterogeneities in orogenic plateau growth: Insights from 3-D thermo-mechanical modeling. *Journal of Geophysical Research: Solid Earth*, 121(4), 3118-3138. https://doi.org/10.1002/2016JB012872

Chen, L., Zhan, Z., & Li, Y. (2016, January). 3D Numerical Modeling on the Present Tectonic Deformation Field in Tibetan Plateau. In *ISRM International Symposium on In-Situ Rock Stress*. International Society for Rock Mechanics and Rock Engineering.

Chen, M., Huang, H., Yao, H., van der Hilst, R., & Niu, F. (2014). Low wave speed zones in the crust beneath SE Tibet revealed by ambient noise adjoint tomography. *Geophysical Research Letters*, 41(2), 334-340. https://doi.org/10.1002/2013GL058476

Chen, M., Niu, F., Tromp, J., Lenardic, A., Lee, C. T. A., Cao, W., & Ribeiro, J. (2017b). Lithospheric foundering and underthrusting imaged beneath Tibet.

Nature communications, 8, 15659. https://doi.org/10.1038/ncomms15659

Chen, Y., & Wu, F. T. (1989). Lancang-Gengma earthquake: A preliminary report on the November 6, 1988, event and its aftershocks. *Eos, Transactions American Geophysical Union*, 70(49), 1527–1540. https://doi.org/10.1029/89EO00376

Chen, Y., Xu, Y., Xu, T., Si, S., Liang, X., Tian, X., ... & Lan, H. (2015). Magmatic underplating and crustal growth in the Emeishan Large Igneous Province, SW China, revealed by a passive seismic experiment. *Earth and Planetary Science Letters*, 432, 103-114. https://doi.org/10.1016/j.epsl.2015.09.048

Chen, Y., Zhang, Z., Sun, C., & Badal, J. (2013). Crustal anisotropy from Moho converted Ps wave splitting analysis and geodynamic implications beneath the eastern margin of Tibet and surrounding regions. *Gondwana Research*, 24(3-4), 946-957. https://doi.org/10.1016/j.gr.2012.04.003

Cheng, Y., Tang, J., Chen, X., Dong, Z., & Wang, L. (2019). Crustal structure and magma plumbing system beneath the Puer Basin, southwest China: Insights from three-dimensional magnetotelluric imaging. *Tectonophysics*, 763, 30-45. https://doi.org/10.1016/j.tecto.2019.04.032

Chevalier, M. L., Leloup, P. H., Replumaz, A., Pan, J., Liu, D., Li, H., ... & Métois, M. (2016). Tectonic-geomorphology of the Litang fault system, SE Tibetan Plateau, and implication for regional seismic hazard. *Tectonophysics*, 682, 278-292. https://doi.org/10.1016/j.tecto.2016.05.039

Clark, M. K., Bush, J. W., & Royden, L. H. (2005). Dynamic topography produced by lower crustal flow against rheological strength heterogeneities bordering the Tibetan Plateau. *Geophysical Journal International*, 162(2), 575-590. https://doi.org/10.1111/j.1365-246X.2005.02580.x

Clark, M. K., & Royden, L. H. (2000). Topographic ooze: Building the eastern margin of Tibet by lower crustal flow. *Geology*, 28(8), 703-706. https://doi.org/10.1130/0091-7613(2000)28<703:TOBTEM>2.0.CO;2

Collettini, C., Niemeijer, A., Viti, C., & Marone, C. (2009). Fault zone fabric and fault weakness. *Nature*, 462(7275), 907. https://doi.org/10.1038/nature08585

Cook, K. L., & Royden, L. H. (2008). The role of crustal strength variations in shaping orogenic plateaus, with application to Tibet. *Journal of Geophysical Research: Solid Earth*, 113(B8). https://doi.org/10.1029/2007JB005457

Deng, Q., Zhang, P., Ran, Y., Yang, X., Min, W., & Chu, Q. (2003). Basic characteristics of active tectonics of China. *Science in China Series D: Earth Sciences*, 46(4), 356-372. https://xs.scihub.ltd/https://doi.org/10.1360/03yd9032

Deng, Y., Li, J., Song, X., & Zhu, L. (2018). Joint inversion for lithospheric structures: Implications for the growth and deformation in Northeastern Tibetan Plateau. *Geophysical Research Letters*, 45(9), 3951-3958. https://doi.org/10.1029/2018GL077486

Diao, F., Wang, R., Wang, Y., Xiong, X., & Walter, T. R. (2018). Fault behavior and lower crustal rheology inferred from the first seven years of postseismic GPS data after the 2008 Wenchuan earthquake. *Earth and Planetary Science Letters*, 495, 202-212. https://doi.org/10.1016/j.epsl.2018.05.020

Dong, H., Wei, W., Jin, S., Ye, G., Zhang, L., Yin, Y., ... & Jones, A. G. (2016).

661 Extensional extrusion: Insights into south-eastward expansion of Tibetan Plateau
662 from magnetotelluric array data. *Earth and Planetary Science Letters*, 454, 78-85.
663 https://doi.org/10.1016/j.epsl.2016.07.043
664 Ekström, G., Nettles, M., & Dziewoński, A. M. (2012). The global CMT project
665 2004–2010: Centroid-moment tensors for 13,017 earthquakes. Physics of the
666 *Earth and Planetary Interiors*, 200, 1-9.
667 https://doi.org/10.1016/j.pepi.2012.04.002
668 England, P., & Molnar, P. (1990). Right-lateral shear and rotation as the explanation
669 for strike-slip faulting in eastern Tibet. *Nature*, 344(6262), 140.
670 https://doi.org/10.1038/344140a0
671 Flesch, L., Bendick, R., & Bischoff, S. (2018). Limitations on inferring 3D
672 architecture and dynamics from surface velocities in the India-Eurasia collision
673 zone. *Geophysical Research Letters*, 45(3), 1379-1386.
674 https://doi.org/10.1002/2017GL076503
675 Flesch, L. M., Haines, A. J., & Holt, W. E. (2001). Dynamics of the India-Eurasia
676 collision zone. *Journal of Geophysical Research: Solid Earth*, 106(B8), 16435-
677 16460. https://doi.org/10.1029/2001JB000208
678 Gan, W., Zhang, P., Shen, Z. K., Niu, Z., Wang, M., Wan, Y., ... & Cheng, J. (2007).
679 Present-day crustal motion within the Tibetan Plateau inferred from GPS
680 measurements. *Journal of Geophysical Research: Solid Earth*, 112(B8).
681 https://doi.org/10.1029/2005JB004120
682 Gao, G., Kang, G., Bai, C., & Wen, L. (2015). Study on crustal magnetic anomalies
683 and Curie surface in Southeast Tibet. *Journal of Asian Earth Sciences*, 97, 169-
684 177. https://doi.org/10.1016/j.jseaes.2014.10.035
685 Gao, X., & Wang, K. (2014). Strength of stick-slip and creeping subduction
686 megathrusts from heat flow observations. *Science*, 345(6200), 1038-1041. doi:
687 10.1126/science.1255487
688 Guo, X., Zhang, L., Su, X., Mao, Z., Gao, X. Y., Yang, X., & Ni, H. (2018). Melting
689 Inside the Tibetan Crust? Constraint From Electrical Conductivity of
690 Peraluminous Granitic Melt. *Geophysical Research Letters*, 45(9), 3906-3913.
691 https://doi.org/10.1029/2018GL077804
692 Hacker, B. R., Ritzwoller, M. H., & Xie, J. (2014). Partially melted, mica-bearing
693 crust in Central Tibet. *Tectonics*, 33(7), 1408-1424.
694 https://doi.org/10.1002/2014TC003545
695 Hemant, K., & Mitchell, A. (2009). Magnetic field modelling and interpretation of the
696 Himalayan–Tibetan Plateau and adjoining north Indian Plains. *Tectonophysics*,
697 478(1-2), 87-99. https://doi.org/10.1016/j.tecto.2009.06.009
698 Hearn, E. H., Bürgmann, R., & Reilinger, R. E. (2002). Dynamics of Izmit earthquake
699 postseismic deformation and loading of the Duzce earthquake hypocenter.
700 *Bulletin of the Seismological Society of America*, 92(1), 172-193.
701 https://doi.org/10.1785/0120000832
702 Hearn, E. H., McClusky, S., Ergintav, S., & Reilinger, R. E. (2009). Izmit earthquake
703 postseismic deformation and dynamics of the North Anatolian Fault Zone.
704 *Journal of Geophysical Research: Solid Earth*, 114(B8).

https://doi.org/10.1029/2008JB006026
Hirth, G., Teyssier, C., & Dunlap, J. W. (2001). An evaluation of quartzite flow laws based on comparisons between experimentally and naturally deformed rocks. *International Journal of Earth Sciences*, 90(1), 77-87. https://doi.org/10.1007/s005310000152
Hu, S., He, L., & Wang, J. (2000). Heat flow in the continental area of China: a new data set. *Earth and Planetary Science Letters*, 179(2), 407-419. https://doi.org/10.1016/S0012-821X(00)00126-6
Huang, M. H., Bürgmann, R., & Freed, A. M. (2014). Probing the lithospheric rheology across the eastern margin of the Tibetan Plateau. *Earth and Planetary Science Letters*, 396, 88-96. https://doi.org/10.1016/j.epsl.2014.04.003
Huang, Z., Wang, L., Xu, M., Ding, Z., Wu, Y., Wang, P., et al. (2015). Teleseismic shear-wave splitting in SE Tibet: Insight into complex crust and upper-mantle deformation. *Earth and Planetary Science Letters*, 432, 354–362. https://doi.org/10.1016/j.epsl.2015.10.027
Huang, Z., Wang, L., Xu, M., & Zhao, D. (2018). P Wave Anisotropic Tomography of the SE Tibetan Plateau: Evidence for the Crustal and Upper-Mantle Deformations. *Journal of Geophysical Research: Solid Earth*, 123(10), 8957-8978. https://doi.org/10.1029/2018JB016048
Jackson, J. A. (2002). Strength of the continental lithosphere: time to abandon the jelly sandwich?. *GSA today*, 12, 4-10.
Jiménez-Munt, I., & Platt, J. P. (2006). Influence of mantle dynamics on the topographic evolution of the Tibetan Plateau: Results from numerical modeling. *Tectonics*, 25(6). https://doi.org/10.1029/2006TC001963
Johnson, K. M., & Segall, P. (2004). Viscoelastic earthquake cycle models with deep stress-driven creep along the San Andreas fault system. *Journal of Geophysical Research: Solid Earth*, 109(B10). https://doi.org/10.1029/2004JB003096
Karato, S. I. (2010). Rheology of the Earth's mantle: A historical review. *Gondwana Research*, 18(1), 17-45. https://doi.org/10.1016/j.gr.2010.03.004
Karato, S. I., & Wu, P. (1993). Rheology of the upper mantle: A synthesis. *Science*, 260(5109), 771-778. doi: 10.1126/science.260.5109.771
Kohlstedt, D. L., Evans, B., & Mackwell, S. J. (1995). Strength of the lithosphere: Constraints imposed by laboratory experiments. *Journal of Geophysical Research: Solid Earth*, 100(B9), 17587-17602. https://doi.org/10.1029/95JB01460
Kreemer, C., Blewitt, G., & Klein, E. C. (2014). A geodetic plate motion and global strain rate model. *Geochemistry, Geophysics, Geosystems*, 15(10), 3849-3889. https://doi.org/10.1002/2014GC005407
Lacassin, R., Maluski, H., Leloup, P. H., Tapponnier, P., Hinthong, C., Siribhakdi, K., et al. (1997). Tertiary diachronic extrusion and deformation of western Indochina: Structural and 40Ar/39Ar evidence from NW Thailand. *Journal of Geophysical Research*, 102(B5), 10,013–10,037. https://doi.org/10.1029/96JB03831
Lacassin, R., Replumaz, A., & Hervé Leloup, P. (1998). Hairpin river loops and slip-sense inversion on southeast Asian strike-slip faults. *Geology*, 26(8), 703–706.

https://doi.org/10.1130/0091-7613(1998)026<0703:HRLASS>2.3.CO;2

Landau, L., and E. Lifshitz (1986), Theory of Elasticity, Butterworth Heinemann, Oxford, U. K

Leloup, P. H., Lacassin, R., Tapponnier, P., Schärer, U., Zhong, D., Liu, X., ... & Trinh, P. T. (1995). The Ailao Shan-Red River shear zone (Yunnan, China), Tertiary transform boundary of Indochina. *Tectonophysics*, 251(1-4), 3-84. https://doi.org/10.1016/0040-1951(95)00070-4

Leng, W., & Gurnis, M. (2011). Dynamics of subduction initiation with different evolutionary pathways. *Geochemistry, Geophysics, Geosystems*, 12(12). https://doi.org/10.1029/2011GC003877

Leng, W., & Gurnis, M. (2015). Subduction initiation at relic arcs. *Geophysical Research Letters*, 42(17), 7014-7021. https://doi.org/10.1002/2015GL064985

Lockner, D. A., Morrow, C., Moore, D., & Hickman, S. (2011). Low strength of deep San Andreas fault gouge from SAFOD core. *Nature*, 472(7341), 82. https://doi.org/10.1038/nature09927

Li, J., Song, X., Zhu, L., & Deng, Y. (2017a). Joint inversion of surface wave dispersions and receiver functions with P velocity constraints: Application to Southeastern Tibet. *Journal of Geophysical Research: Solid Earth*, 122(9), 7291-7310. https://doi.org/10.1002/2017JB014135

Li, X., Bai, D., Ma, X., Chen, Y., Varentsov, I. M., Xue, G., ... & Lozovsky, I. (2019a). Electrical resistivity structure of the Xiaojiang strike-slip fault system (SW China) and its tectonic implications. *Journal of Asian Earth Sciences*, 176, 57-67. https://doi.org/10.1016/j.jseaes.2019.01.031

Li, Y., Chen, L., Tan, P., & Li, H. (2014). Lower crustal flow and its relation to the surface deformation and stress distribution in western Sichuan region, China. *Journal of Earth Science*, 25(4), 630-637. https://doi.org/10.1007/s12583-014-0467-x

Li, Y., Jia, D., Shaw, J. H., Hubbard, J., Lin, A., Wang, M., ... & Wu, L. (2010). Structural interpretation of the coseismic faults of the Wenchuan earthquake: Three-dimensional modeling of the Longmen Shan fold-and-thrust belt. *Journal of Geophysical Research: Solid Earth*, 115(B4). https://doi.org/10.1029/2009JB006824

Li, Y., Liu, M., Li, Y., & Chen, L. (2019b). Active crustal deformation in southeastern Tibetan Plateau: The kinematics and dynamics. *Earth and Planetary Science Letters*, 523, 115708. https://doi.org/10.1016/j.epsl.2019.07.010

Li, Y., Liu, S., Chen, L., Du, Y., Li, H., & Liu, D. (2017b). Mechanism of crustal deformation in the Sichuan-Yunnan region, southeastern Tibetan Plateau: Insights from numerical modeling. *Journal of Asian Earth Sciences*, 146, 142-151. https://doi.org/10.1016/j.jseaes.2017.05.018

Liang, S., Gan, W., Shen, C., Xiao, G., Liu, J., Chen, W., ... & Zhou, D. (2013). Three-dimensional velocity field of present-day crustal motion of the Tibetan Plateau derived from GPS measurements. *Journal of Geophysical Research: Solid Earth*, 118(10), 5722-5732. https://doi.org/10.1002/2013JB010503

Liu-Zeng, J., Tapponnier, P., Gaudemer, Y., & Ding, L. (2008). Quantifying landscape differences across the Tibetan plateau: Implications for topographic relief evolution. *Journal of Geophysical Research: Earth Surface*, 113(F4). https://doi.org/10.1029/2007JF000897

Luo, G., & Liu, M. (2018). Stressing Rates and Seismicity on the Major Faults in Eastern Tibetan Plateau. *Journal of Geophysical Research: Solid Earth*, 123(12), 10-968. https://doi.org/10.1029/2018JB015532

Magni, V., Faccenna, C., van Hunen, J., & Funiciello, F. (2014). How collision triggers backarc extension: Insight into Mediterranean style of extension from 3-D numerical models. *Geology*, 42(6), 511-514. https://doi.org/10.1130/G35446.1

Maurin, T., Masson, F., Rangin, C., Min, U. T., & Collard, P. (2010). First global positioning system results in northern Myanmar: Constant and localized slip rate along the Sagaing fault. *Geology*, 38(7), 591-594. https://doi.org/10.1130/G30872.1

Meade, B. J., & Loveless, J. P. (2009). Block modeling with connected fault-network geometries and a linear elastic coupling estimator in spherical coordinates. *Bulletin of the Seismological Society of America*, 99(6), 3124-3139. https://doi.org/10.1785/0120090088

Moresi, L., Zhong, S., & Gurnis, M. (1996). The accuracy of finite element solutions of Stokes's flow with strongly varying viscosity. *Physics of the Earth and Planetary Interiors*, 97(1-4), 83-94. https://doi.org/10.1016/0031-9201(96)03163-9

Moresi, L., Dufour, F., & Mühlhaus, H. B. (2003). A Lagrangian integration point finite element method for large deformation modeling of viscoelastic geomaterials. *Journal of computational physics*, 184(2), 476-497. https://doi.org/10.1016/S0021-9991(02)00031-1

Niemeijer, A., Marone, C., & Elsworth, D. (2010). Frictional strength and strain weakening in simulated fault gouge: Competition between geometrical weakening and chemical strengthening. *Journal of Geophysical Research: Solid Earth*, 115(B10). https://doi.org/10.1029/2009JB000838

Okada, Y. (1985). Surface deformation due to shear and tensile faults in a half-space. *Bulletin of the seismological society of America*, 75(4), 1135-1154.

Pan, G., Wang, L., & Zhu, D. (2004). Thoughts on some important scientific problems in regional geological survey of the Qinghai-Tibet Plateau [J]. *Regional Geology of China*, 1, 12-19.

Panda, D., Kundu, B., & Santosh, M. (2018). Oblique convergence and strain partitioning in the outer deformation front of NE Himalaya. *Scientific reports*, 8(1), 10564. https://doi.org/10.1038/s41598-018-28774-3

Panda, D., Mondal, A., & Kundu, B. (2019). Eastward "glacier-like flow" of the Tibetan crust constrained from power-law rheology. *Journal of Asian Earth Sciences*, 177, 129-133. https://doi.org/10.1016/j.jseaes.2019.03.021

Pasyanos, M. E., Masters, T. G., Laske, G., & Ma, Z. (2014). LITHO1. 0: An updated crust and lithospheric model of the Earth. *Journal of Geophysical Research: Solid Earth*, 119(3), 2153-2173. https://doi.org/10.1002/2013JB010626

Peltzer, G., & Tapponnier, P. (1988). Formation and evolution of strike-slip faults, rifts, and basins during the India-Asia collision: An experimental approach. Journal of Geophysical Research: Solid Earth, 93(B12), 15085-15117.

Poliakov, A. N., & Buck, W. R. (1998). Mechanics of stretching elastic-plastic-viscous layers: Applications to slow-spreading mid-ocean ridges. *Geophysical Monograph-American Geophysical Union*, 106, 305-324.

Ren, J., Xu, X., Yeats, R. S., & Zhang, S. (2013). Latest Quaternary paleoseismology and slip rates of the Longriba fault zone, eastern Tibet: Implications for fault behavior and strain partitioning. *Tectonics*, 32(2), 216-238. https://doi.org/10.1002/tect.20029

Rippe, D., & Unsworth, M. (2010). Quantifying crustal flow in Tibet with magnetotelluric data. *Physics of the Earth and Planetary Interiors*, 179(3-4), 107-121. https://doi.org/10.1016/j.pepi.2010.01.009

Royden, L. H., Burchfiel, B. C., King, R. W., Wang, E., Chen, Z., Shen, F., & Liu, Y. (1997). Surface deformation and lower crustal flow in eastern Tibet. *science*, 276(5313), 788-790. doi: 10.1126/science.276.5313.788

Royden, L. H., Burchfiel, B. C., & van der Hilst, R. D. (2008). The geological evolution of the Tibetan Plateau. *science*, 321(5892), 1054-1058. doi: 10.1126/science.1155371

Rutter, E. H., & Brodie, K. H. (2004). Experimental grain size-sensitive flow of hot-pressed Brazilian quartz aggregates. *Journal of Structural Geology*, 26(11), 2011-2023. https://doi.org/10.1016/j.jsg.2004.04.006

Rutter, E. H., Brodie, K. H., & Irving, D. H. (2006). Flow of synthetic, wet, partially molten “granite” under undrained conditions: an experimental study. *Journal of Geophysical Research: Solid Earth*, 111(B6). https://doi.org/10.1029/2005JB004257

Rybacki, E., Gottschalk, M., Wirth, R., & Dresen, G. (2006). Influence of water fugacity and activation volume on the flow properties of fine-grained anorthite aggregates. *Journal of Geophysical Research: Solid Earth*, 111(B3). https://doi.org/10.1029/2005JB003663

Savage, J. C., & Burford, R. O. (1973). Geodetic determination of relative plate motion in central California. *Journal of Geophysical Research*, 78(5), 832-845. https://doi.org/10.1029/JB078i005p00832

Schoenbohm, L. M., Burchfiel, B. C., Liangzhong, C., & Jiyun, Y. (2006). Miocene to present activity along the Red River fault, China, in the context of continental extrusion, upper-crustal rotation, and lower-crustal flow. *Geological Society of America Bulletin*, 118(5-6), 672-688. https://doi.org/10.1130/B25816.1

Shao, Z., Wang, R., Wu, Y., & Zhang, L. (2011). Rapid afterslip and short-term viscoelastic relaxation following the 2008 M W 7.9 Wenchuan earthquake. *Earthquake Science*, 24(2), 163-175. https://doi.org/10.1007/s11589-010-0781-z

Shen, W., Ritzwoller, M. H., Kang, D., Kim, Y., Lin, F. C., Ning, J., ... & Zhou, L. (2016). A seismic reference model for the crust and uppermost mantle beneath China from surface wave dispersion. *Geophysical Journal International*, 206(2), 954-979. https://doi.org/10.1093/gji/ggw175

Shen, Z. K., Lü, J., Wang, M., & Bürgmann, R. (2005). Contemporary crustal deformation around the southeast borderland of the Tibetan Plateau. *Journal of Geophysical Research: Solid Earth*, 110(B11). https://doi.org/10.1029/2004JB003421

Shi, F. (2014). Tectonic geomorphology of the Nantinghe Fault in Southwestern Yunnan. PhD thesis (in Chinese with English abstract). Institute of Geology, China Earthquake Administration Beijing.

Shi, X., Kirby, E., Furlong, K. P., Meng, K., Robinson, R., & Wang, E. (2015). Crustal strength in central Tibet determined from Holocene shoreline deflection around Siling Co. *Earth and Planetary Science Letters*, 423, 145-154. https://doi.org/10.1016/j.epsl.2015.05.002

Shi, X., Wang, Y., Sieh, K., Weldon, R., Feng, L., Chan, C. H., & Liu-Zeng, J. (2018). Fault slip and GPS velocities across the Shan Plateau define a curved southwestward crustal motion around the eastern Himalayan syntaxis. *Journal of Geophysical Research: Solid Earth*, 123(3), 2502-2518. https://doi.org/10.1002/2017JB015206

Smith-Konter, B. R., Sandwell, D. T., & Shearer, P. (2011). Locking depths estimated from geodesy and seismology along the San Andreas Fault System: Implications for seismic moment release. *Journal of Geophysical Research: Solid Earth*, 116(B6). https://doi.org/10.1029/2010JB008117

Socquet, A., & Pubellier, M. (2005). Cenozoic deformation in western Yunnan (China–Myanmar border). *Journal of Asian Earth Sciences*, 24(4), 495-515. https://doi.org/10.1016/j.jseaes.2004.03.006

Sternai, P., Avouac, J. P., Jolivet, L., Faccenna, C., Gerya, T., Becker, T. W., & Menant, A. (2016). On the influence of the asthenospheric flow on the tectonics and topography at a collision-subduction transition zones: Comparison with the eastern Tibetan margin. *Journal of Geodynamics*, 100, 184-197. https://doi.org/10.1016/j.jog.2016.02.009

Sun, X., Bao, X., Xu, M., Eaton, D. W., Song, X., Wang, L., ... & Li, H. (2014). Crustal structure beneath SE Tibet from joint analysis of receiver functions and Rayleigh wave dispersion. *Geophysical Research Letters*, 41(5), 1479-1484. https://doi.org/10.1002/2014GL059269

Tackley, P. J. (2000). Self-consistent generation of tectonic plates in time-dependent, three-dimensional mantle convection simulations 2. Strain weakening and asthenosphere. *Geochemistry, Geophysics, Geosystems*, 1(8). https://doi.org/10.1029/2000GC000043

Takei, Y. (2002). Effect of pore geometry on Vp/Vs: From equilibrium geometry to crack. *Journal of Geophysical Research: Solid Earth*, 107(B2), ECV-6. ttps://doi.org/10.1029/2001JB000522

Tao, K., Grand, S. P., & Niu, F. (2018). Seismic structure of the upper mantle beneath Eastern Asia from full waveform seismic tomography. *Geochemistry, Geophysics, Geosystems*, 19(8), 2732-2763. https://doi.org/10.1029/2018GC007460

Tapponnier, P., Peltzer, G. L. D. A. Y., Le Dain, A. Y., Armijo, R., & Cobbold, P.

(1982). Propagating extrusion tectonics in Asia: New insights from simple experiments with plasticine. *Geology*, 10(12), 611-616. https://doi.org/10.1130/0091-7613(1982)10<611:PETIAN>2.0.CO;2

Tapponnier, P., Zhiqin, X., Roger, F., Meyer, B., Arnaud, N., Wittlinger, G., & Jingsui, Y. (2001). Oblique stepwise rise and growth of the Tibet Plateau. *science*, 294(5547), 1671-1677. doi: 10.1126/science.105978

Taylor, M., & Yin, A. (2009). Active structures of the Himalayan-Tibetan orogen and their relationships to earthquake distribution, contemporary strain field, and Cenozoic volcanism. *Geosphere*, 5(3), 199-214. https://doi.org/10.1130/GES00217.1

Tunini, L., Jiménez-Munt, I., Fernandez, M., Vergés, J., & Bird, P. (2017). Neotectonic deformation in central Eurasia: A geodynamic model approach. *Journal of Geophysical Research: Solid Earth*, 122(11), 9461-9484. https://doi.org/10.1002/2017JB014487

Wang, E. (Ed.). (1998). *Late Cenozoic Xianshuihe-Xiaojiang, Red River, and Dali fault systems of southwestern Sichuan and central Yunnan, China* (Vol. 327). Geological Society of America.

Wang, J. H., Yin, A., Harrison, T. M., Grove, M., Zhang, Y. Q., & Xie, G. H. (2001). A tectonic model for Cenozoic igneous activities in the eastern Indo–Asian collision zone. *Earth and Planetary Science Letters*, 188(1-2), 123-133. https://doi.org/10.1016/S0012-821X(01)00315-6

Wang, J. Y., & Huang, S. P. (1987). Linear relationship between heat flow and heat production in Panxi Paleorift Zone, southwestern China. *Geophysical Research Letters*, 14(3), 272-274. https://doi.org/10.1029/GL014i003p00272

Wang, Q., Xu, X., Shyu, J. B. H., Jiang, Z., Liu, S., Wu, Y., ... & Wei, W. (2019). Viscoelastic behavior of the crust around the Longmenshan Thrust Belt inferred from post-seismic deformation of the 2013 Lushan earthquake, China. *Journal of Asian Earth Sciences*, 173, 386-396. https://doi.org/10.1016/j.jseaes.2019.02.001

Wang, W., Qiao, X., Yang, S., & Wang, D. (2016). Present-day velocity field and block kinematics of Tibetan Plateau from GPS measurements. *Geophysical Journal International*, 208(2), 1088-1102. https://doi.org/10.1093/gji/ggw445

Wang, W., Wu, J., Fang, L., Lai, G., Yang, T., & Cai, Y. (2014). S wave velocity structure in southwest China from surface wave tomography and receiver functions. *Journal of Geophysical Research: Solid Earth*, 119(2), 1061-1078. https://doi.org/10.1002/2013JB010317

Wang, Y. (2001). Heat flow pattern and lateral variations of lithosphere strength in China mainland: constraints on active deformation. *Physics of the Earth and Planetary Interiors*, 126(3-4), 121-146. https://doi.org/10.1016/S0031-9201(01)00251-5

Wang, Y., Zhang, X., Jiang, C., Wei, H., & Wan, J. (2007). Tectonic controls on the late Miocene–Holocene volcanic eruptions of the Tengchong volcanic field along the southeastern margin of the Tibetan plateau. *Journal of Asian Earth Sciences*, 30(2), 375-389. https://doi.org/10.1016/j.jseaes.2006.11.005

Wei, W., Zhao, D., & Xu, J. (2013). P-wave anisotropic tomography in Southeast

Tibet: New insight into the lower crustal flow and seismotectonics. *Physics of the Earth and Planetary Interiors*, 222, 47-57. https://doi.org/10.1016/j.pepi.2013.07.002

Wu, T., Zhang, S., Li, M., Qin, W., & Zhang, C. (2016). Two crustal flowing channels and volcanic magma migration underneath the SE margin of the Tibetan Plateau as revealed by surface wave tomography. *Journal of Asian Earth Sciences*, 132, 25-39. https://doi.org/10.1016/j.jseaes.2016.09.017

Wu, X., Xu, X., Yu, G., Cheng, J., Chen, G., An, Y., & W, Q. (2018). The map of surface rupture of national earthquake experiment field in Chuan-Dian. Seismology and Geology, 40(1), 27-41. (in Chinese)

Xu, C. J., Fan, Q. B., Wang, Q., Yang, S. M., & Jiang, G. Y. (2014). Postseismic deformation after 2008 wenchuan earthquake. *Survey Review*, 46(339), 432-436. https://doi.org/10.1179/1752270614Y.0000000128

Xu, X., Keller, G. R., Gao, R., Guo, X., & Zhu, X. (2016). Uplift of the Longmen Shan area in the eastern Tibetan Plateau: an integrated geophysical and geodynamic analysis. *International Geology Review*, 58(1), 14-31. https://doi.org/10.1080/00206814.2015.1055595

Xu, X., Wen, X., Han, Z., Chen, G., Li, C., Zheng, W., ... & Wei, Z. (2013). Lushan M S 7.0 earthquake: A blind reserve-fault event. *Chinese Science Bulletin*, 58(28-29), 3437-3443. https://doi.org/10.1007/s11434-013-5999-4

Xu, X., Wen, X., Yu, G., Chen, G., Klinger, Y., Hubbard, J., & Shaw, J. (2009). Coseismic reverse-and oblique-slip surface faulting generated by the 2008 Mw 7.9 Wenchuan earthquake, China. *Geology*, 37(6), 515-518. https://doi.org/10.1130/G25462A.1

Xu, X., Wen, X., Yu, G., Zheng, R., Luo, H., & Zheng, B. (2005). Average slip rate, earthquake rupturing segmentation and recurrence behavior on the Litang fault zone, western Sichuan Province, China. *Science in China Series D: Earth Sciences*, 48(8), 1183-1196. https://doi.org/10.1360/04yd0072

Xue, S., Bai, D., Chen, Y., Ma, X., Chen, L., Li, X., & Yan, Y. (2019). Contrasting crustal deformation mechanisms in the Longmenshan and West Qinling orogenic belts, NE Tibet, revealed by magnetotelluric data. *Journal of Asian Earth Sciences*, 176, 120-128. https://doi.org/10.1016/j.jseaes.2019.01.039

Yang, H., & Duan, Y. (2019). High-resolution crustal structure illuminated by ultra-dense array recordings. *Acta Geologica Sinica-English Edition*, 93, 284-284.

Yang, T., Wu, J., Fang, L., & Wang, W. (2014). Complex Structure beneath the Southeastern Tibetan Plateau from Teleseismic P-Wave Tomography. *Bulletin of the Seismological Society of America*, 104(3), 1056-1069. https://doi.org/10.1785/0120130029

Yang, Y., & Liu, M. (2009). Crustal thickening and lateral extrusion during the Indo-Asian collision: A 3D viscous flow model. *Tectonophysics*, 465(1-4), 128-135. https://doi.org/10.1016/j.tecto.2008.11.002

Yang, Y., Yao, H., Wu, H., Zhang, P., & Wang, M. (2020). A new crustal shear-velocity model in Southwest China from joint seismological inversion and its implications for regional crustal dynamics. *Geophysical Journal International*,

220(2), 1379-1393. https://doi.org/10.1093/gji/ggz514

Yao, H., Van Der Hilst, R. D., & Montagner, J. P. (2010). Heterogeneity and anisotropy of the lithosphere of SE Tibet from surface wave array tomography. *Journal of Geophysical Research: Solid Earth*, 115(B12). https://doi.org/10.1029/2009JB007142

Yin, A., & Harrison, T. M. (2000). Geologic evolution of the Himalayan-Tibetan orogen. *Annual review of earth and planetary sciences*, 28(1), 211-280. https://doi.org/10.1146/annurev.earth.28.1.211

Yin, A., & Taylor, M. H. (2011). Mechanics of V-shaped conjugate strike-slip faults and the corresponding continuum mode of continental deformation. *GSA Bulletin*, 123(9-10), 1798-1821. https://doi.org/10.1130/B30159.1

Yin, F., Jiang, C., Jia, K., Han, L., & Zhang, H. (2019). A study on seismicity in the Yunnan region by using the multidimensional stress release model. *Physics of the Earth and Planetary Interiors*, 289, 115-122. https://doi.org/10.1016/j.pepi.2019.01.007

Zhang, C., Cao, J., & Shi, Y. (2009). Studying the viscosity of lower crust of Qinghai-Tibet Plateau according to post-seismic deformation. *Science in China Series D: Earth Sciences*, 52(3), 411-419. https://doi.org/10.1007/s11430-009-0028-9

Zhang, P., Deng, Q., Zhang, G., Ma, J., Gan, W., Min, W., ... & Wang, Q. (2003). Active tectonic blocks and strong earthquakes in the continent of China. *Science in China Series D: Earth Sciences*, 46(2), 13-24. https://doi.org/10.1360/03dz0002

Zhang, S., & Liu, B. (1978). Seismic characteristicis of Tonghai earthquake in 1970 (in Chinese with English abstract). *Scientia Geologica Sinica*, (4), 323–335.

Zhao, G., Unsworth, M. J., Zhan, Y., Wang, L., Chen, X., Jones, A. G., ... & Li, T. (2012). Crustal structure and rheology of the Longmenshan and Wenchuan Mw 7.9 earthquake epicentral area from magnetotelluric data. *Geology*, 40(12), 1139-1142. https://doi.org/10.1130/G33703.1

Zhao, L. F., Xie, X. B., He, J. K., Tian, X., & Yao, Z. X. (2013). Crustal flow pattern beneath the Tibetan Plateau constrained by regional Lg-wave Q tomography. *Earth and Planetary Science Letters*, 383, 113-122. https://doi.org/10.1016/j.epsl.2013.09.038

Zhao, Y., Ye, G., Dong, J. E., Wei, W., & Jin, S. (2019). Electrical Constraints on the channel flow underneath the northeastern Tibetan plateau: Results of the Longriba-Minjiang magnetotelluric sounding profile. *Journal of Asian Earth Sciences*, 170, 73-83. https://doi.org/10.1016/j.jseaes.2018.10.004

Zheng, G., Wang, H., Wright, T. J., Lou, Y., Zhang, R., Zhang, W., ... & Wei, N. (2017). Crustal deformation in the India-Eurasia collision zone from 25 years of GPS measurements. *Journal of Geophysical Research: Solid Earth*, 122(11), 9290-9312. https://doi.org/10.1002/2017JB014465

Zhu, A., Zhang, D., & Jiang, C. (2016). Numerical simulation of the segmentation of the stress state of the Anninghe-Zemuhe-Xiaojiang faults. *Science China Earth Sciences*, 59(2), 384-396. https://doi.org/10.1007/s11430-015-5157-8

Zhu, S., & Zhang, P. (2013). FEM simulation of interseismic and coseismic

deformation associated with the 2008 Wenchuan Earthquake. *Tectonophysics*, 584, 64-80. https://doi.org/10.1016/j.tecto.2012.06.024

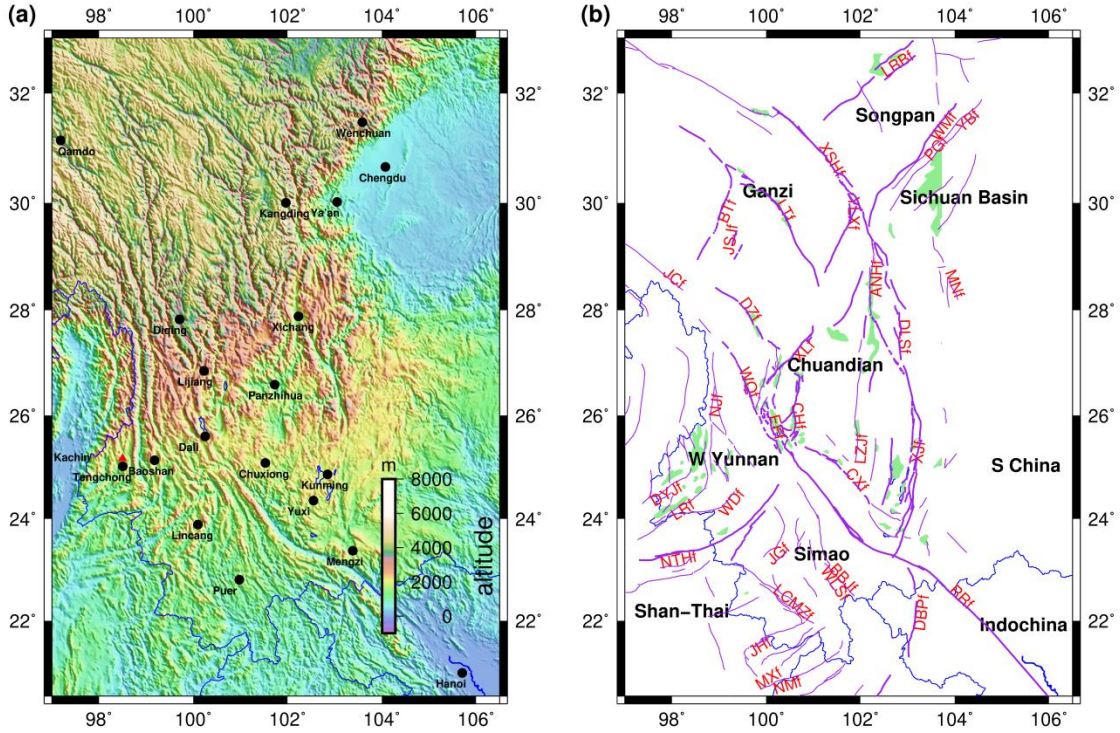

Figure 1. (**a**) Topography (ETOPO5, National Geophysical Data Center, 1993) of SE Tibet, with the cities by the black dots and the volcano indicated by the red triangle. (**b**) Faults and blocks in southeastern Tibet. The purple lines indicate the map of geological fault segments (Zhang et al., 2003; Taylor & Yin, 2009; Wu et al., 2018; Shi et al., 2018) and basins (green shading, provided by the Earth Observation from Space Data Sub-center, http://data.cea-ies.ac.cn). The name and Abbreviations are listed below. ANHf—Anninghe fault; BBJf—Babianjiang fault; BTf—Batang fault; CHf—Chenghai fault; CXf—Chuxiong fault; DBPf—Dien Bien Phu fault; DLSf—Daliangshan fault; DYJf—Dayingjiang fault; DZf—Deqing-Zhongdian fault; EEf—Erhai-Eryuan fault; JGf—Jinggu fault; JHf—Jinghong fault; JSJf—Jinshajiang fault; LRBf—Longriba fault; LCMZf—

1071 Lancang-Mengzhe fault; LRf—Longling-Ruili fault; LTf—Litang fault; LZJf—
1072 Lvzhijiang fault; MNf—Manao fault; MXf—Mengxing fault; NJf—Nujiang
1073 fault; NMf—Nam Ma fault; NTHf—Nantinghe fault; PGf—Pengguan fault;
1074 RRf—Red River fault; WDf—Wanding fault; WLSf—Wuliangshan fault;
1075 WMf—Wenchuan-Maowen fault; WQf—Weixi-Qiaohou fault; XJf—Xiaojiang
1076 fault; XLf—Xiaojinhe-Lijiang fault; XSHf—Xianshuihe fault; YBf—Yingxiu-
1077 Beichuan fault; YLXf—Yulongxi fault.

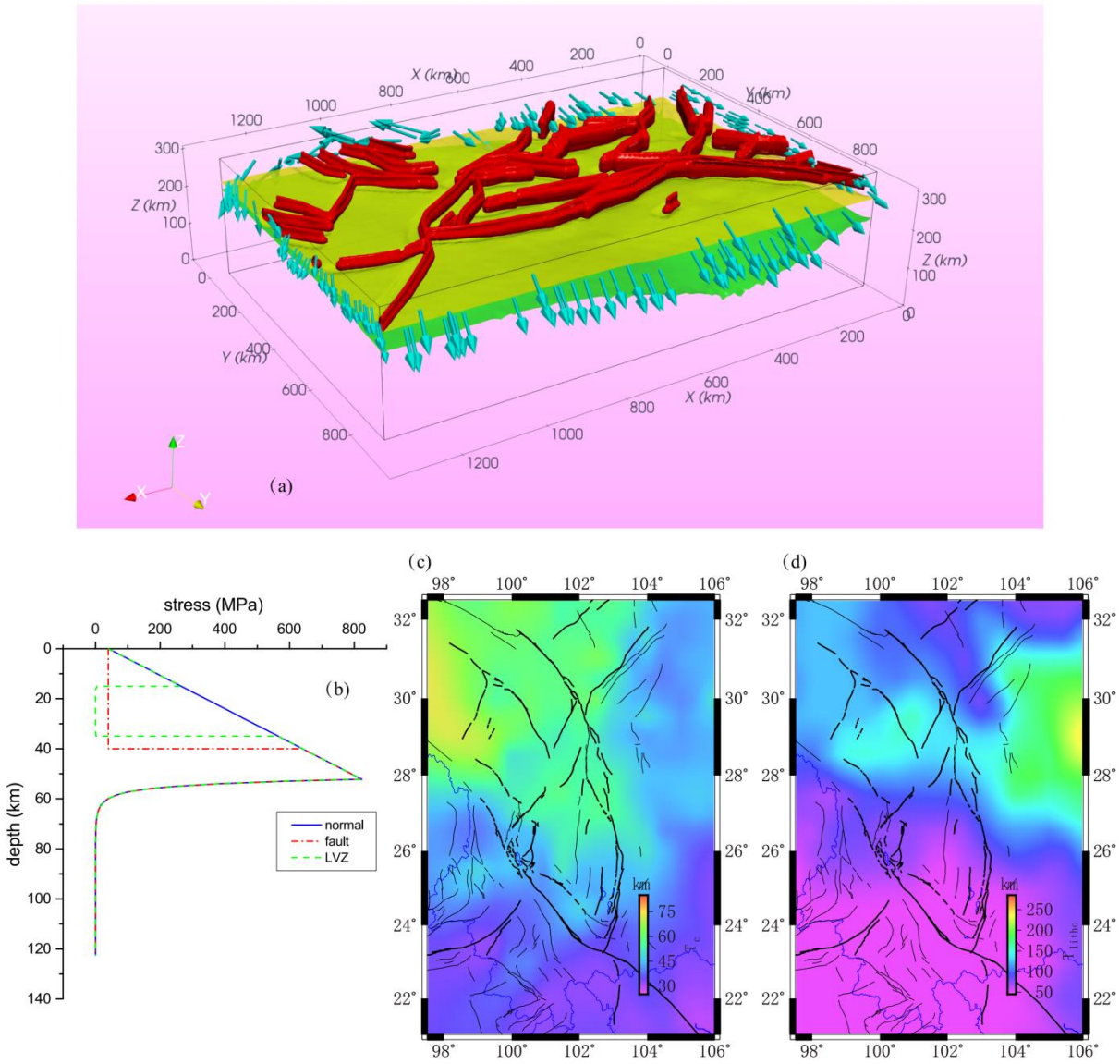

1078

Figure 2. (**a**) The geodynamic model of SE Tibet with faulted shear zones (red), Moho (yellow), LAB (green), and imposed velocity boundary conditions at the surrounding margin of the entire lithosphere (blue). Axis x: south; axis y: east; axis z: upwards. (**b**) Sketches of strength vs. depth. The blue solid line shows the profile for areas without faulted shear zone or an LVZ layer; the red dashed-dotted line shows the profile for areas with faulted shear zones down to the Moho; the green dashed line shows the profile for areas with an extra LVZ layer from 15 km to 35 km, with a viscosity of 10^{20} Pa·s. The Moho depth is set to be 40 km; the frictional coefficient, initial cohesion of friction, μ and C_0, are set to 0.5 and 40 MPa, respectively. The other parameters for rheology are listed in Table 1. For all depths, the reference strain rate is constant at 10^{-15} s^{-1}. (**c**) Moho depth, from Yang et al. (2020). (**d**) Lithosphere thickness, from Litho_1.0 (Pasyanos et al., 2014).

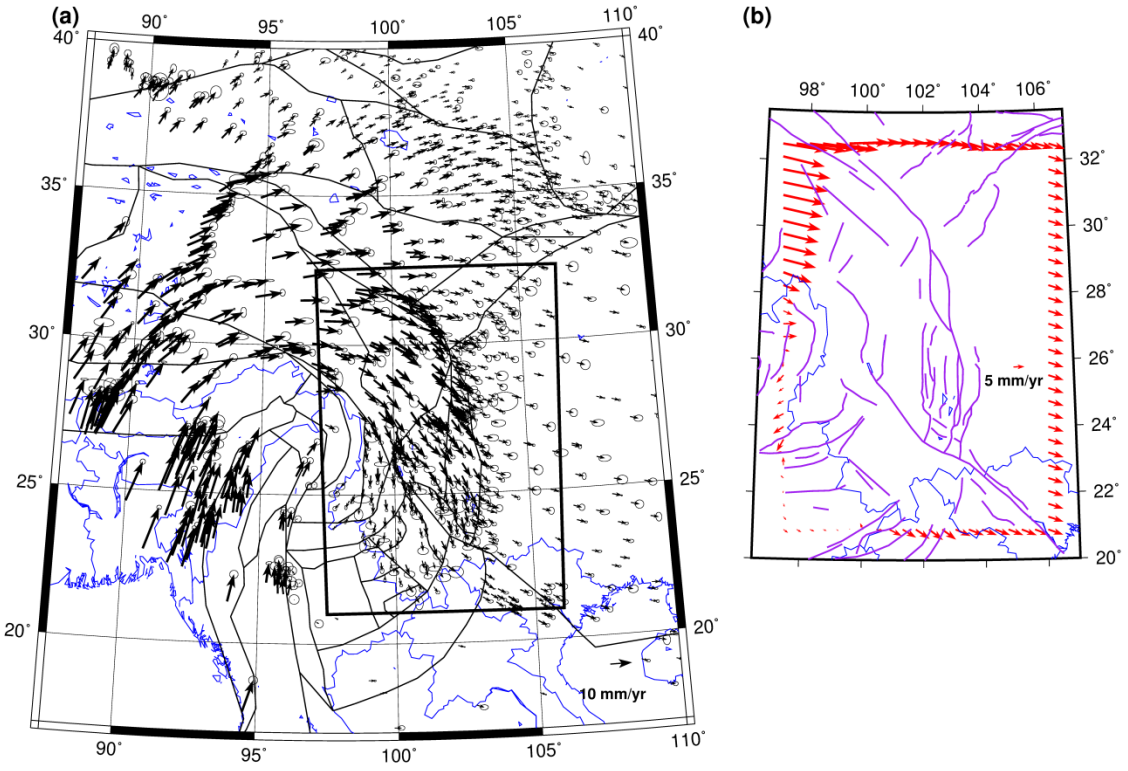

Figure 3. (**a**) Interseismic (25 years) GPS data (black vectors), from Zheng et al. (2017), in the reference frame of stable Eurasian Plate. The black rectangle indicates the study area. (**b**) The lateral velocity boundary conditions used in the model, which are computed based on the Blocks model of Meade & Loveless (2009), in which we used a fault-block network (thin solid black lines in **a**) based on the fault traces from Taylor & Yin (2009) (purple lines in **b**).

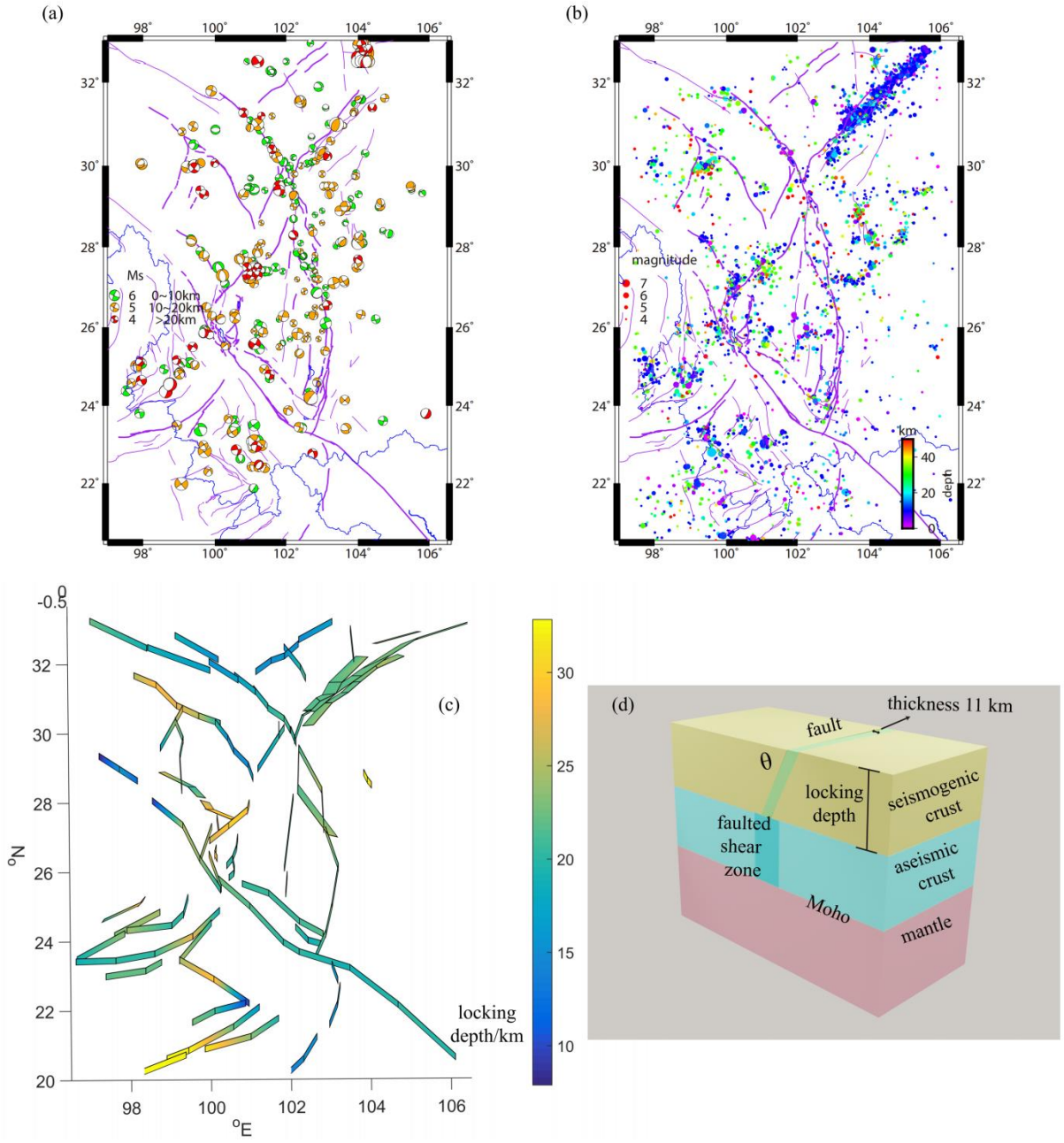

Figure 4. (**a**) Map of the focal mechanism in SE Tibet from the China Earthquake Data Center, from 1966 to 2015, which was used to estimate the dip angle of the adjacent faults. The magnitudes and depth ranges of earthquakes are given in the legend. (**b**) Map of earthquake locations from IRIS (http://ds.iris.edu/wilber3/), from 1968 to 2018, with magnitude > 4. The magnitude and depth are scaled in the colored map and legend. (**c**) 3D fault model (upper part only) in SE Tibet

used in this study, constrained by earthquake locations, focal mechanisms, and geological studies of faults, with strike, dip angle, and locking depth (scaled by the colored map). The selected faults were all active in the Holocene. (**d**) Sketch of the structure of the faulted shear zone. The upper part of faulted shear zone has a thickness of 11 km and θ represents the dip angle; a thicker faulted shear zone is shown from the locking depth to Moho depth.

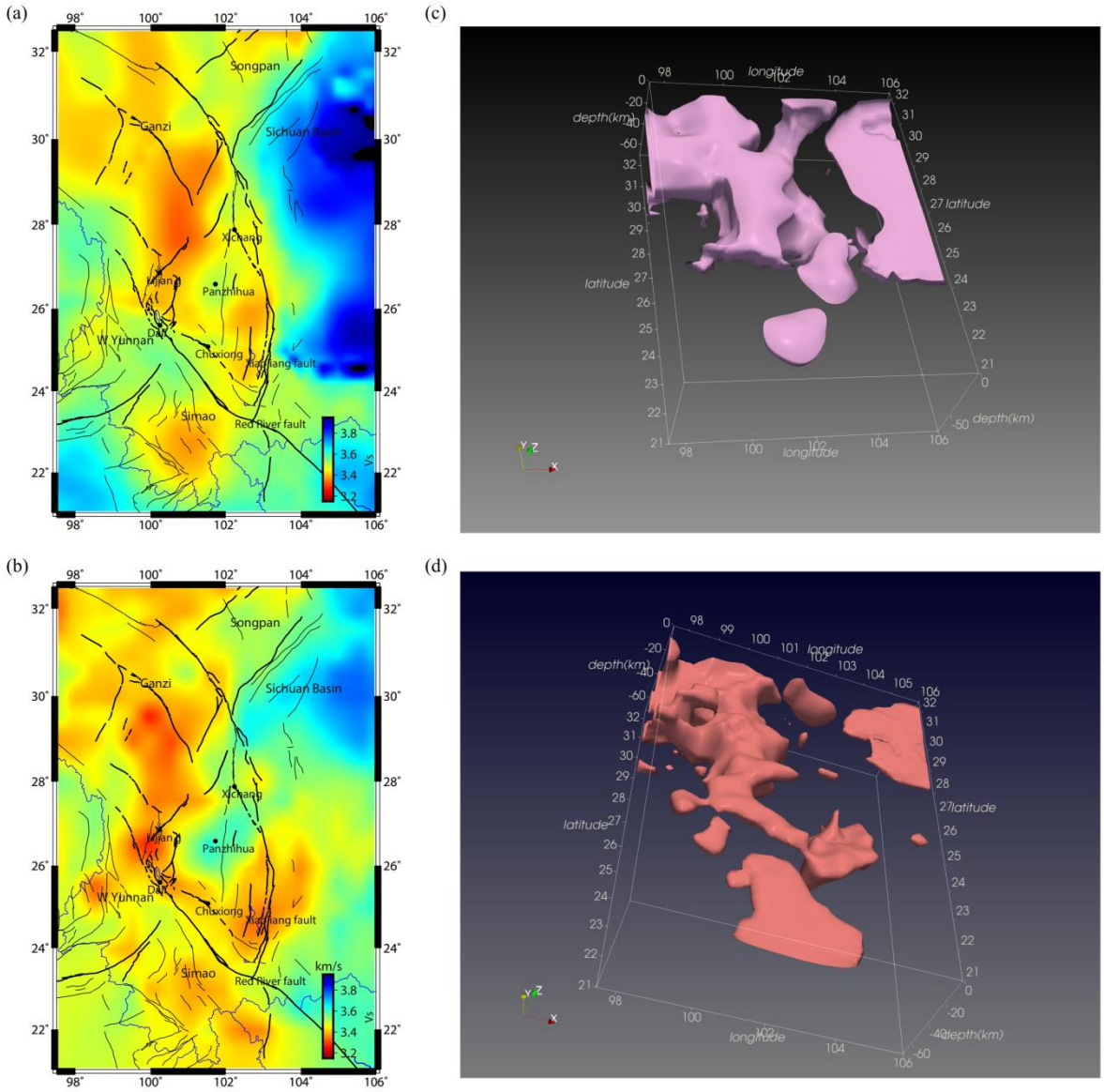

Figure 5. S-wave tomography at the depth of 15 km, from Tao et al. (2018) (**a**) and

Shen et al. (2016) (**b**). 3D illustration of crustal LVZs outlined, based on Tao et al. (2018) (**c**) and Shen et al. (2016) (**d**). The shallow part (~0-10 km) of the low S-wave velocity zone in the Sichuan Basin is the sediment layer and was removed in our geodynamic model.

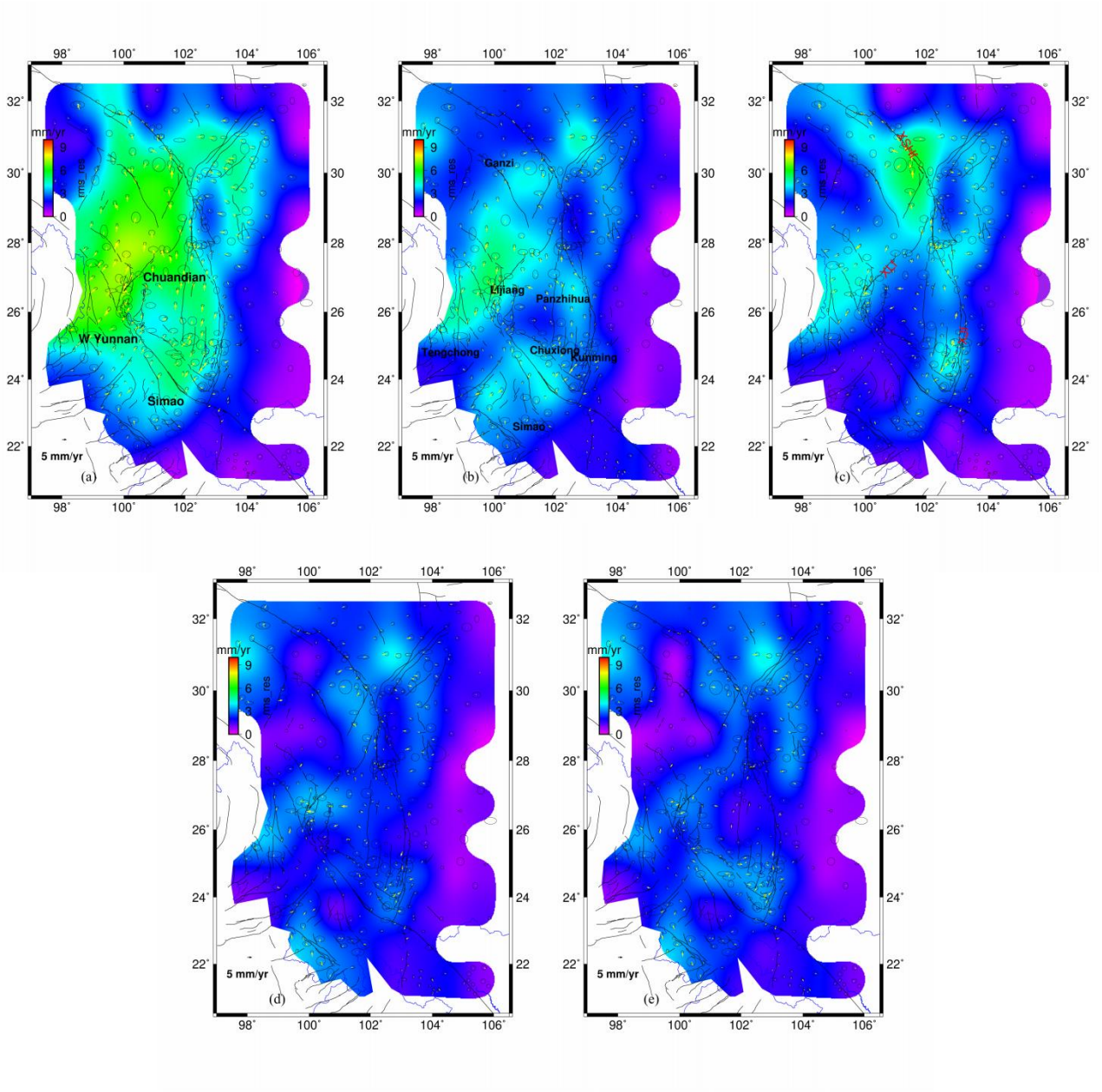

Figure 6. Maps of the distribution of the RMS (root mean square) of residual velocities in SE Tibet resulting from the five models in Table 2. For each GPS

station, the residual velocity (yellow arrows) equals the modeled velocity minus the observed velocity. The distribution of the scale of residual velocity is smoothed, mapped, and colored for each figure. (**a**) Model without faults and LVZs (case_ref); the RMS of the residual velocity is ~4.3 mm/yr. (**b**) Model with faults (case_fault); the RMS of the residual velocity is ~3.1 mm/yr. The area with anomalous velocities in (**b**) coincides with the approximate regime of the LVZs from seismic tomography. (**c**) Model with LVZs only (case_LVZs); the RMS of the residual velocity is ~3.2 mm/yr. The area with anomalous velocities in (**c**) coincides with the area of the Xianshuihe-Xiaojiang fault (XSHf and XJf) and the Xiaojinhe-Lijiang fault (XLf), which have large slip rates. (**d**) Model with both faults and LVZs (case_both1) based on Tao et al. (2018); the RMS of the residual velocity is ~2.5 mm/yr. (**e**) Model with both faults and LVZs (case_both2) based on Shen et al. (2016); the RMS of the residual velocity is ~2.5 mm/yr.

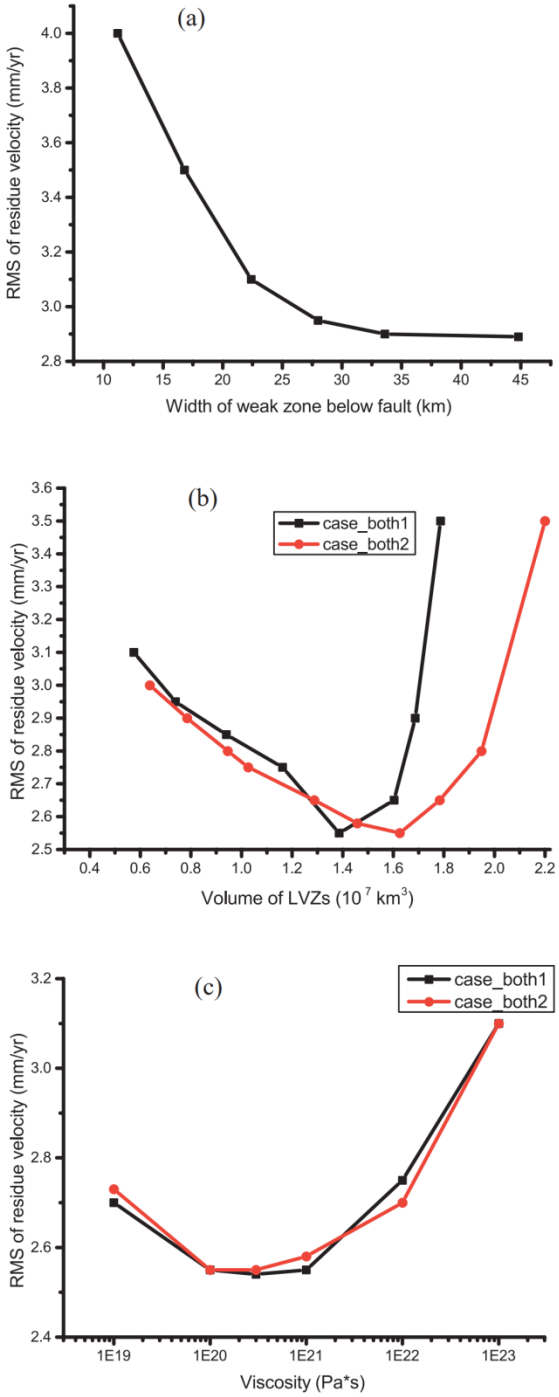

Figure 7. (**a**) RMS of residual velocity vs. the thickness of the lower faulted shear zones for case_fault. (**b**) RMS of the residual velocity vs. the volume of LVZs for case_both1 (Tao et al., 2018) and case_both2 (Shen et al., 2016). (**c**) RMS of residual velocity vs. viscosity of LVZs for case_both1 and case_both2.

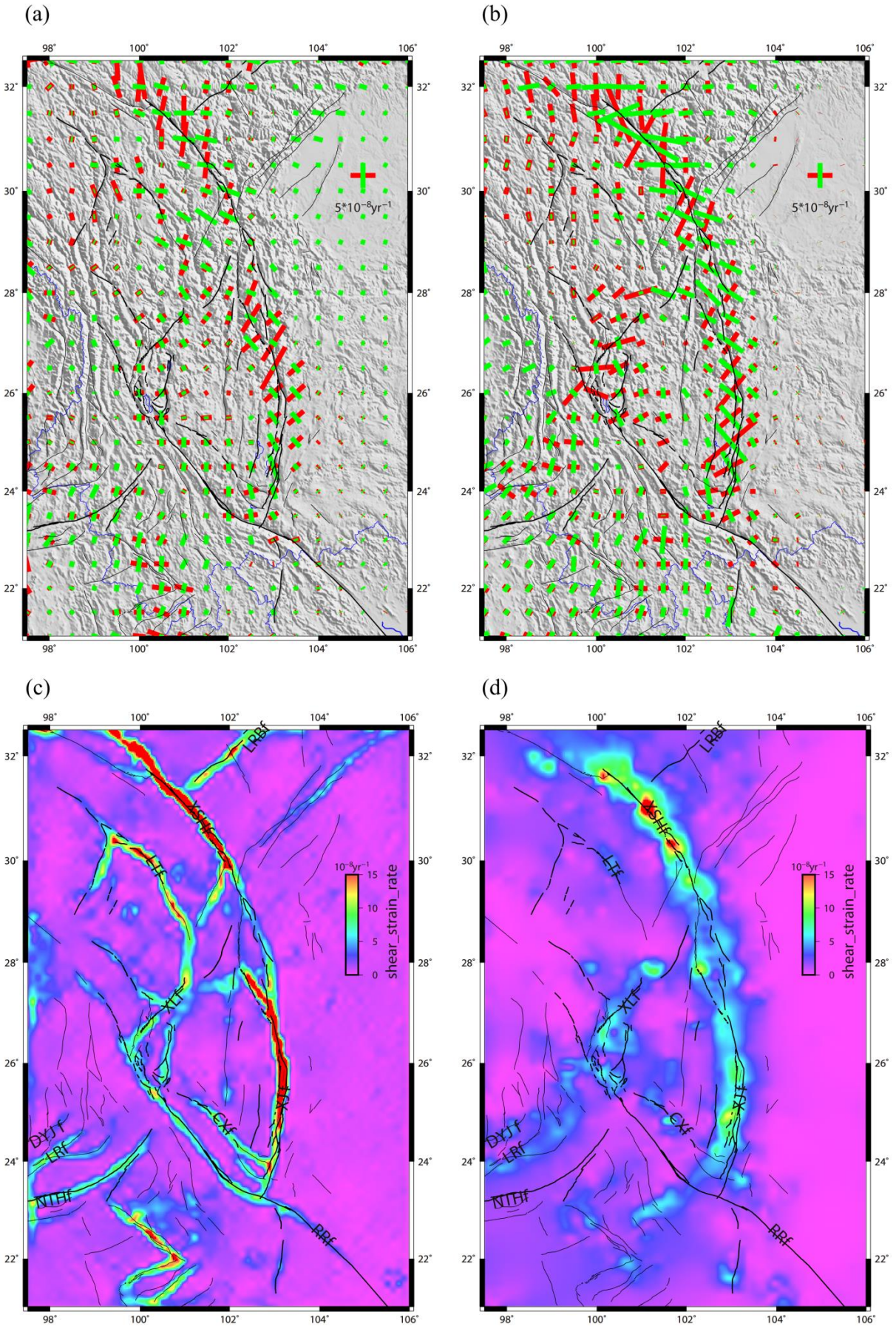
(a)
(b)
(c)
(d)
98°
100°
102°
104°
106°
32°
30°
28°
26°
24°
22°
5*10⁻⁸yr⁻¹
LRBf
XSHf
LTf
XLTf
CKf
DYJf
LRf
NTHf
RRf
10⁻⁸yr⁻¹
15
10
5
0
shear_strain_rate

1140

Figure 8. Distributions of the strain rate tensor (**a**) and maximum shear strain rate (**c**) for case_both1 with faults and LVZs; maps of strain rate tensor (**b**) and maximum shear strain rate (**d**) calculated from smoothed observed GPS data for SE Tibet (Kreemer et al., 2014). In (**a**) and (**b**), red represents extensional and green represents compressional strain rate. In (**c**) and (**d**), CXf—Chuxiong fault; DYJf—Dayingjiang fault; LRf—Longling-Ruili fault; LRBf—Longriba fault; LTf—Litang fault; NTHf—Nantinghe fault; RRf—Red River fault; XLf—Xiaojinhe-Lijiang fault; XJf—Xiaojiang fault; XSHf—Xianshuihe fault.

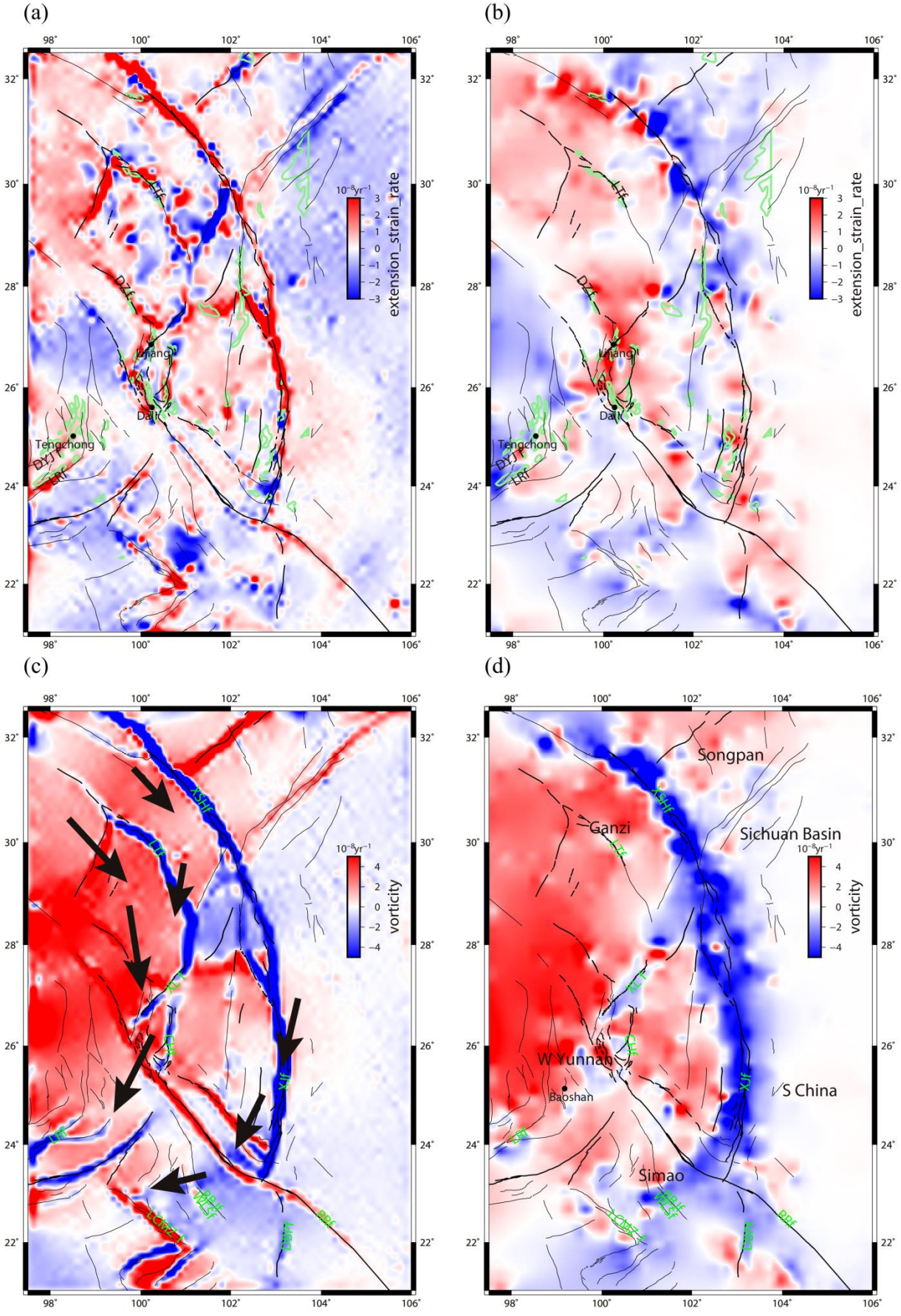
(a)
(b)
(c)
(d)
extension_strain_rate
vorticity
$10^{-8}yr^{-1}$
Songpan
Ganzi
Sichuan Basin
W Yunnan
S China
Simao
Baoshan
Tengchong
Dali
Lijiang
XSHF
LTF
DZF
XJF
CHF
DYJF
LRF
RRF
WLSF
LCHMZF
BRF
LXJF

Figure 9. Distribution of expansion strain rate (**a**) and vorticity (**c**) for case_both1 with faults and LVZs; maps of expansion strain rate (**b**) and vorticity (**d**) calculated from smoothed observed GPS data for SE Tibet (Kreemer et al., 2014). In (**a**) and (**b**), most basins (green outlines; available through http://data.cea-ies.ac.cn) are under an extensional environment except for the Sichuan Basin (expansion: red, compression: blue). In (**c**) and (**d**), the strike-slip senses of all faults agree with geological records (Clockwise/right lateral: red, anti-clockwise/left lateral: blue). Two channel flows occur in the LVZs, the directions of which are represented by black arrows. BBJf—Babianjiang fault; CHf—Chenghai fault; DBPf—Dien Bien Phu fault; DZf—Deqing-Zhongdian fault; DYJf—Dayingjiang fault; LCMZf—Lancang-Mengzhe fault; LRf—Longling-Ruili fault; LRBf—Longriba fault; LTf—Litang fault; NTHf—Nantinghe fault; RRf—Red River fault; WLSf—Wuliangshan fault; XLf—Xiaojinhe-Lijiang fault; XJf—Xiaojiang fault; XSHf—Xianshuihe fault.

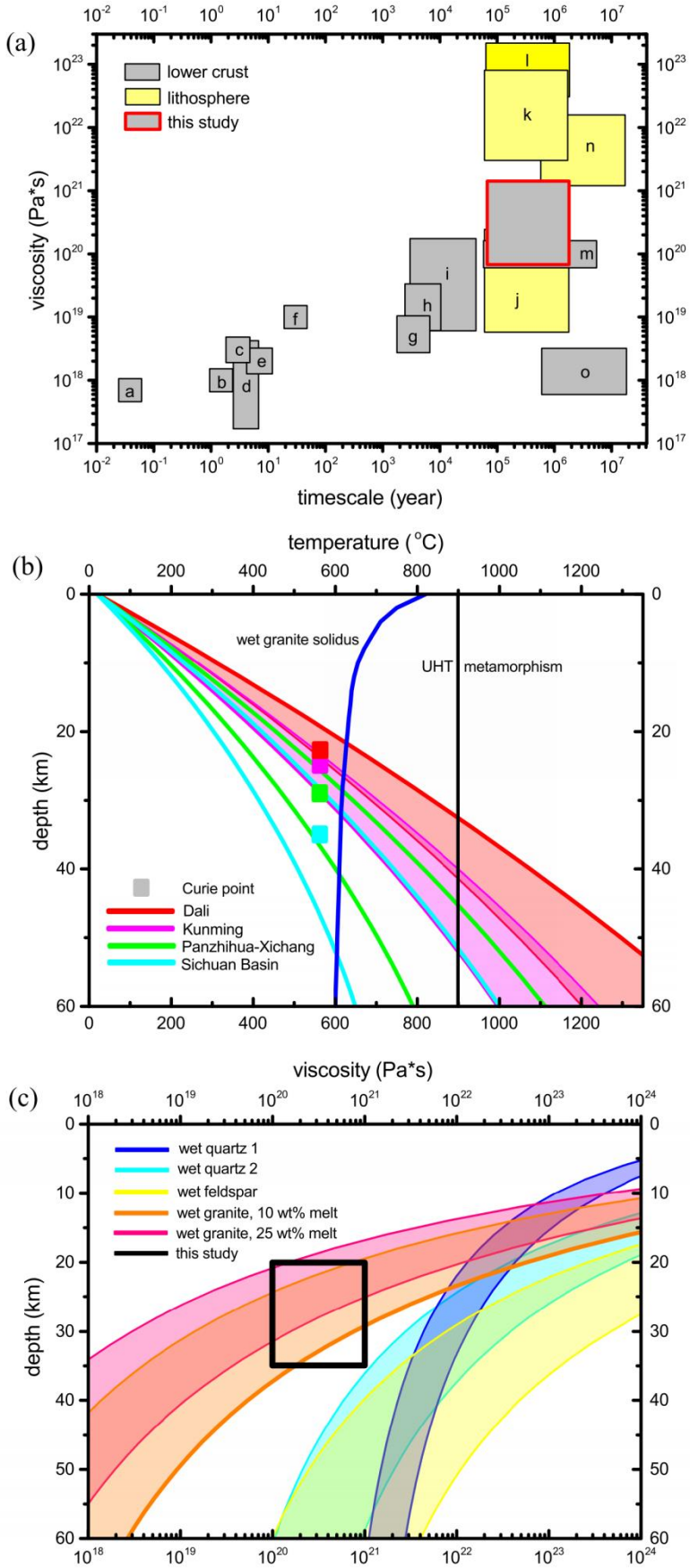
(a)
lower crust
lithosphere
this study
viscosity (Pa*s)
timescale (year)
a
b
c
d
e
f
g
h
i
j
k
l
m
n
o
(b)
temperature (°C)
wet granite solidus
UHT metamorphism
depth (km)
Curie point
Dali
Kunming
Panzhihua-Xichang
Sichuan Basin
(c)
viscosity (Pa*s)
depth (km)
wet quartz 1
wet quartz 2
wet feldspar
wet granite, 10 wt% melt
wet granite, 25 wt% melt
this study

Figure 10. (**a**) Viscosity of mid-lower crust (gray) or entire lithosphere (yellow) in SE Tibet constrained by previous geodynamic modeling over different timescales (based on Huang et al. (2014) and Panda et al. (2019)). Postseismic: a-Shao et al. (2011); b-Huang et al. (2014); c-Xu et al. (2014); d-Wang et al. (2019); e-Diao et al. (2018); f-Zhang et al. (2009); Earthquake cycle: g-Zhu & Zhang (2013); Lake-shoreline rebound: h-Shi et al. (2015); i-England et al. (2013); Geodynamic: j-Yin & Taylor (2011); k-Flesch et al. (2001); l-Panda et al. (2019); m-Bischoff & Flesch (2018); Topographic: n-Jiménez-Munt & Platt (2006); o-Clark & Royden (2000) and Xu et al. (2016). (**b**) Temperature profiles for the area with LVZs (Kunming and Dali) and without LVZs (the Sichuan Basin and Panzhihua-Xichang). Squares indicate the depth of the Curie surface (Gao et al., 2015). Thin light blue and black lines represent curves of wet granite solidus and ultrahigh temperature metamorphism, respectively. (**c**) Viscosity profiles based on the temperature of two LVZs from the temperature profiles (**b**), of wet quartzite (deep blue/wet quartz 1: Hirth et al., 2001; light blue/wet quartz 2: Rutter & Brodie, 2004), wet feldspar (yellow: Rybacki et al., 2006), and partially molten wet granite (Rutter et al., 2006) with a melt fraction of 10wt% (orange) and 25wt% (pink). Nonlinear flow laws are used and the reference strain rate is 1×10^{-15} s^{-1}.

1187 **Table 1.** Constants used in the model.

X length	1294 km
Y width	884 km
Z depth	302 km
D_{air} air layer thickness	20 km
G shear modulus	3×10^{10} Pa
Ra Rayleigh number	5×10^{7}
α thermal expansion coefficient	3×10^{-5} K^{-1}
η_0 reference mantle viscosity	1×10^{19} Pa·s
κ_0 reference thermal diffusivity	1×10^{-6} W/m·K
C_0 initial plastic yield stress	40 MPa
C_f minimum plastic yield stress	0.6 MPa
ε_f reference plastic strain	0.3
T_0 reference temperature	1500 K
R gas constant	8.31 $J\cdot K^{-1}$ mol^{-1}
E activation energy	540 kJ/mol
μ coefficient of friction	0.5
n strain exponent	3.5
$\dot{\varepsilon}_0$ reference strain rate	1×10^{-15} s^{-1}

1188

1189 **Table 2.** Cases in Figure 6 and parameters used in these cases.

Name	Fault included	LVZs included	LVZs model	thickness of weak zone below the fault (km)	Ratio r of LVZs	Viscosity of LVZs (Pa·s)	RMS of residual velocity (mm/yr)
case_ref	no	no					~4.3
case_fault	yes	no		22			~3.1
case_LVZs	no	yes	Tao_2018		0.7	10^{20}	~3.2
case_both1	yes	yes	Tao_2018	22	0.7	10^{20}	~2.5
case_both2	yes	yes	Shen_2016	22	0.4	10^{20}	~2.5

1190